Experimental observation of oscillatory cellular patterns in three-dimensional directional solidification

J. Pereda, F.L. Mota, Lin Chen, B. Billia, D. Tourret, Y. Song, J.-M. Debierre, R. Guerin, A. Karma, R. Trivedi, et al.

To cite this version:

J. Pereda, F.L. Mota, Lin Chen, B. Billia, D. Tourret, et al.. Experimental observation of oscillatory cellular patterns in three-dimensional directional solidification. Physical Review E , 2017, 95 (1), pp.012803. 10.1103/PhysRevE.95.012803 . hal-01637150

HAL Id: hal-01637150
https://hal.science/hal-01637150v1

Submitted on 17 Nov 2017

PHYSICAL REVIEW E **95**, 012803 (2017)

Experimental observation of oscillatory cellular patterns in three-dimensional directional solidification

J. Pereda,[1] F. L. Mota,[1] L. Chen,[1] B. Billia,[1] D. Tourret,[2] Y. Song,[2] J.-M. Debierre,[1] R. Guérin,[1] A. Karma,[2]
R. Trivedi,[3] and N. Bergeon[1,*]
[1]*Institut Matériaux Microélectronique Nanosciences de Provence, Aix-Marseille Université and CNRS UMR 7334, Campus Saint-Jérôme, Case 142, 13397 Marseille Cedex 20, France*
[2]*Department of Physics and Center for Interdisciplinary Research on Complex Systems, Northeastern University, Boston, Massachusetts 02115, USA*
[3]*Department of Materials Science and Engineering, Iowa State University, Ames, Iowa 50010, USA*

(Received 4 November 2016; published 13 January 2017)

We present a detailed analysis of oscillatory modes during three-dimensional cellular growth in a diffusive transport regime. We ground our analysis primarily on *in situ* observations of directional solidification experiments of a transparent succinonitrile 0.24 wt% camphor alloy performed in microgravity conditions onboard the International Space Station. This study completes our previous reports [Bergeon *et al.*, Phys. Rev. Lett. **110**, 226102 (2013); Tourret *et al.*, Phys. Rev. E **92**, 042401 (2015)] from an experimental perspective, and results are supported by additional phase-field simulations. We analyze the influence of growth parameters, crystal orientation, and sample history on promoting oscillations, and on their spatiotemporal characteristics. Cellular patterns display a remarkably uniform oscillation period throughout the entire array, despite a high array disorder and a wide distribution of primary spacing. Oscillation inhibition may be associated to crystalline disorientation, which stems from polygonization and is manifested as pattern drifting. We determine a drifting velocity threshold above which oscillations are inhibited, thereby demonstrating that inhibition is due to cell drifting and not directly to disorientation, and also explaining the suppression of oscillations when the pulling velocity history favors drifting. Furthermore, we show that the array disorder prevents long-range coherence of oscillations, but not short-range coherence in localized ordered regions. For regions of a few cells exhibiting hexagonal (square) ordering, three (two) subarrays oscillate with a phase shift of approximately ±120° (180°), with square ordering occurring preferentially near subgrain boundaries.

DOI: 10.1103/PhysRevE.95.012803

I. INTRODUCTION

The topic of pattern formation is of paramount importance in many scientific fields, and the process of pattern selection is quite complex since it occurs in a highly nonlinear growth regime [1]. During directional solidification of alloys, the interface between the solid and the melt exhibits complex patterns that are analogous to patterns that form in other fields, such as combustion, fluid dynamics, geology, and biology. Thus, an understanding of solidification patterns provides a general theoretical framework that is useful for a broad class of pattern formation in nature. Moreover, the microstructure formed in the solid largely controls its mechanical properties so that further understanding of the basic physical principles that govern microstructure formation during solidification directly benefits to the improvement of materials processing [2,3].

In directional solidification of binary alloys, the planar solid-liquid interface bifurcates into a cellular structure when the morphological instability parameter, proportional to $V_i C_i / G$ with V_i the interface growth velocity, C_i the liquid concentration at the interface and G the thermal gradient, exceeds a critical value. Pattern selection actually occurs under dynamic growth conditions in which the unstable pattern reorganizes into a rather periodic array.

In situ observation of the solid-liquid interface is a valuable tool to obtain a detailed knowledge of the entire time evolution of the interface pattern. For this reason, extensive use has been made of transparent organic analogs that solidify like metallic alloys but are transparent to visible light, so that the dynamics of the solid-liquid interface can be observed using classical optical techniques [4–11]. Most experimental studies with transparent systems have been performed using a thin sample configuration, the interface being observed from the side. In that case, a single row of cells or dendrites forms along the width of the sample, and the pattern observed from the top (liquid side) can be considered a one-dimensional array. Even if for a sample thickness larger than ≈25 μm, tip shapes are three dimensional [12], such thin samples correspond to a "confined three-dimensional" configuration and the pattern will be referred to as one dimensional (1D) thereafter. Added to the relative simplicity of the experimental and optical systems in such a configuration, another major advantage is the drastic reduction of convection in the melt, which is known to strongly affect microstructural pattern formation [13–17]. Even if studies in thin samples have led to significant advances in understanding the dynamics of solidification, quantitative data extracted from thin samples often cannot be extrapolated to large 3D bulk samples [12,18,19]. The growth process in a large 3D sample leads to the formation of extended 2D arrays. The geometrical characteristics, defects, and neighbor interactions between cells are more complex in 2D arrays formed in bulk samples than in 1D arrays formed in thin samples. In spite of its importance, the dynamics of extended 3D patterns still remains poorly characterized and understood. This is largely due to the experimental

---

[*] nathalie.bergeon@im2np.fr

difficulty of *in situ* observation in bulk samples and the necessity of eliminating fluid flow effects, which requires the reduced-gravity environment of space. The present study was conducted on board the International Space Station (ISS) in the framework of the French Space Agency (CNES) project MISOL3D (Microstructures de Solidification 3D) and NASA project DSIP (Dynamical Selection of Interface Patterns). Experiments were realized using the directional solidification insert (DSI) of the device for the study of critical liquids and crystallization (DECLIC) developed by CNES which is dedicated to *in situ* and real-time characterization of the dynamical selection of the solid-liquid interface morphology on bulk samples of transparent materials [20–23].

Systematic studies of pattern formation and dynamics were conducted in directional solidification of a succinonitrile-camphor alloy for various thermal gradients G and pulling velocities V (the solute concentration C_0 of the sample is fixed). In the cellular regime, as growth progresses, the interface pattern evolves to organize both in terms of spacing adjustment and ordering [23]. The cellular or dendritic patterns may undergo secondary instability in domains of control parameters where other branches of microstructures are more stable, and thus form preferentially. A diversity of secondary instabilities can be found in spatially modulated interface patterns [24,25], but a number of them occur in a narrow range of growth conditions so that their observation is not straightforward. In a recent paper [26], we reported the unprecedented observation of an oscillatory instability in spatially extended 2D cellular patterns. This type of secondary instability, often termed "vacillating-breathing mode" has been experimentally and theoretically studied in thin samples for both cellular [27–29] and two-phase eutectic interfaces [30–32], and theoretically predicted for 3D cellular growth [33,34]. Regarding eutectic systems, one may distinguish between lamellar and rod morphologies that correspond to drastically different patterns in thick samples. A recent study of Perrut *et al.* [35] reports oscillation in the disordered hexagonal based rodlike pattern which is formed in thick samples of transparent alloys. An experimental characterization of the oscillating mode of cellular patterns was done for a 1D cellular pattern by Georgelin and Pocheau [28] in thin samples of transparent alloys. Our experiments revealed extended cellular patterns oscillating with periods of a few tens of minutes. In combination with the experiments, dedicated large-scale phase-field simulations produced breathing modes of comparable characteristics in terms of period as well as in terms of spatiotemporal coherence. We recently presented a phase-field numerical study of these oscillating patterns [36]. In the following, we present the results of a more in-depth analysis of experimentally observed oscillating patterns and supplement the interpretation of those observations by additional phase-field simulations. The results shed light on the growth conditions that favor oscillations and the inhibitory role of crystal disorientation.

In the first part of this paper (Sec. II), we describe the experimental device as well as the procedures that we apply to statistically characterize the pattern in terms of primary spacing and level of disorder. We also present the experimental procedures specifically developed for the analysis of oscillating patterns. Next, in Sec. III we present the analysis of results. General characteristics of oscillation patterns, including spatial ordering and the relationships between local order and oscillation coherence, are first presented in Sec. III A. Section III B then discusses the conditions for the occurrence of oscillations including the role of tip splitting and pattern drifting of tilted cells. Conclusions are summarized in Sec. IV.

II. EXPERIMENTAL PROCEDURE

A. Directional solidification device DECLIC-DSI

The DSI of the DECLIC facility includes a Bridgman type furnace and the experimental cartridge; more complete descriptions of DECLIC and its inserts can be found elsewhere [20,21]. The Bridgman furnace is composed of a hot zone and a cold zone located at the top and bottom of the adiabatic zone, respectively, so that a temperature gradient G can be generated (between 10 and 30 K/cm). Solidification is performed by pulling the experimental cartridge containing the alloy from the hot zone towards the cold zone at a constant pulling rate V (between 0.1 and 30 μm/s). The experimental cartridge comprises the quartz crucible and a system of volume compensation made of stainless steel that is mandatory to accommodate the specimen volume variations associated with phase changes. The cylindrical crucible has an inner diameter of 10 mm and a length that enables about 10 cm of solidification, allowing the study of the whole development of extended 2D patterns from their initial stages up to the permanent regime of growth morphology. The crucible is equipped with a flat glass window at the bottom and a lens immersed in the melt at the top. The main observation mode takes advantage of the complete axial transparency of the cartridge provided by these last two elements: the light coming from light-emitting diodes (LEDs) passes through the cartridge from the bottom to the top, crossing the interface of which the image is formed on a charge-coupled device (CCD) camera; these top-view images of the microstructure are used to study array dynamics and characteristics. On the same cartridge axis, a Mach-Zehnder interferometer is also set using a He-Ne laser. The principles of the analysis of the interferometric images can be found in [37]. In the transverse observation mode, the light coming from two LEDs crosses the sample from one side to the other, which provides a real-time control of interface position and curvature (side-view image). In the current article, images obtained by the direct axial and transverse observations are analyzed.

The organic transparent alloy used is a succinonitrile (SCN) camphor, with a nominal concentration $C_0 = 0.24$ wt % camphor. The alloy was prepared with SCN purified by NASA by successive distillation and zone melting. Every step of sample preparation was carefully realized under vacuum to avoid humidity contamination. A single crystalline solid seed with a direction $\langle 100\rangle$ parallel to the pulling axial direction was prepared on ground and kept during all the experimental campaigns. Further details about the experimental procedure can be found in previous works [23,38].

No direct *in situ* measurement of the thermal gradient is available in the DSI as no thermocouple is inserted inside the sample to avoid thermal perturbations. Control temperatures are imposed to the regulating areas but these areas are not in contact with the cartridge as a gap of 1 mm is necessary for cartridge manipulations. Additionally, the cylindrical geometry and the conductivity difference between the quartz crucible and the alloy result in a complex thermal field that is difficult to characterize. The thermal gradient is estimated using software packages CRYSVUN® and CRYSMAS® which are designed for the global modeling of solidification processes in complex furnaces with axial or translational symmetry [39]. Two different sets of control temperatures were used that correspond to two different thermal gradients, estimated by thermal numerical simulation at $G_1 = 19\,\mathrm{K/cm}$ and $G_2 = 12\,\mathrm{K/cm}$. A more complete discussion of the thermal gradient determination can be found in [40]. A range of pulling velocities from 0.25 to 30 $\mu\mathrm{m/s}$ was studied which covers a range of microstructures from planar to cellular and dendritic.

B. Pattern characterization

In situ continuous observation led to a large amount of images: systematic procedures had to be developed and validated to extract relevant quantitative data. An example of raw image is given in Fig. 1(a). Quantitative characterization of the patterns consists of measuring the evolution, as a function of time and control parameters, of the parameters that describe the interface morphology, such as the primary spacing and the order or disorder level of pattern. Image treatment and analysis procedures have been developed using several software packages (such as VISILOG® or IMAGEJ) to facilitate exploitation of results.

Primary spacing corresponds to the center-to-center distance between two first-neighbor cells in top-view images. Successive operations aiming at enhancing the cell outlines are applied to obtain an exploitable binary image. Image treatment is then applied to sharpen the boundaries between adjacent cells to single lines: the cell center is determined and each cell is tagged. Segments linking adjacent cells are measured so that a histogram of the first-neighbor distances can be drawn to determine the average spacing and its standard deviation. Additionally, the position of each cell center is followed through time to evidence cell dynamics and pattern drift. The number of nearest neighbors is also determined; it gives information on the quantity of topological defects in the pattern.

C. Oscillation characterization by top-view observation

In top-view images [see Fig. 1(a) for example], cells appear bright due to the light guided through their body. A few bottoms of cell grooves also appear bright but in most cases, the position of the groove is defined as the dark line separating bright areas. The size of the bright area will be called "apparent cell area" in the following. Two videos of oscillating patterns are given as Supplemental Material [41], corresponding to top-view observations at $V = 0.75$ (video 1) and 1 (video 2) $\mu\mathrm{m/s}$ ($G_1 = 19\,\mathrm{K/cm}$). On these top-view images, oscillating cells are characterized by a periodic variation of their apparent area.

A method was developed to measure the variation of apparent area $A_i(t)$ of each cell over a large interface area to characterize oscillation. All measurements are done with the VISILOG® software with macroprocedures specifically developed to tackle large numbers of images.

Starting with the first raw image of a sequence [Fig. 1(a), extracted from video 2 attached in the Supplemental Material], each initial grey-level image is transformed into a binary image ensuring that a large majority of cells are disconnected from their neighbors [Fig. 1(b)]. At this step, a few cells having

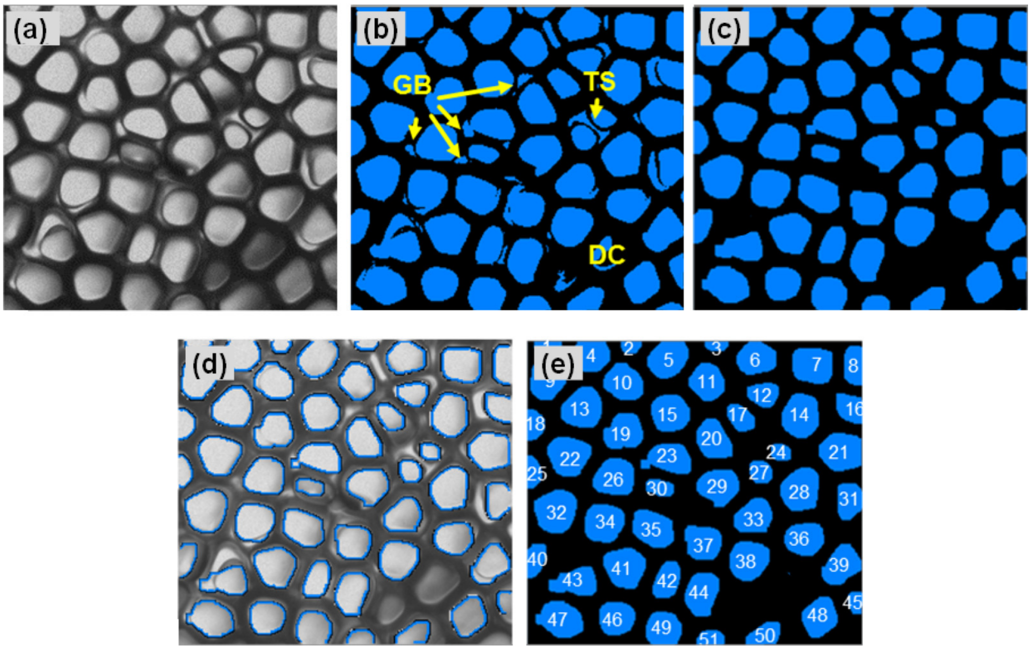

FIG. 1. (a) Example of an initial raw image ($3.2 \times 3.2\,\mathrm{mm}^2$). (b) Binary image evidencing some defects resulting from dark cells (DC), tip-splitting events (TS), or groove bottoms (GB). (c) Binary image after processing with "opening function". (d) Contours of apparent cell area on corrected binary image superimposed on the initial raw image. (e) Tagged binary image ($V = 1\,\mu\mathrm{m/s}$, $G_1 = 19\,\mathrm{K/cm}$).

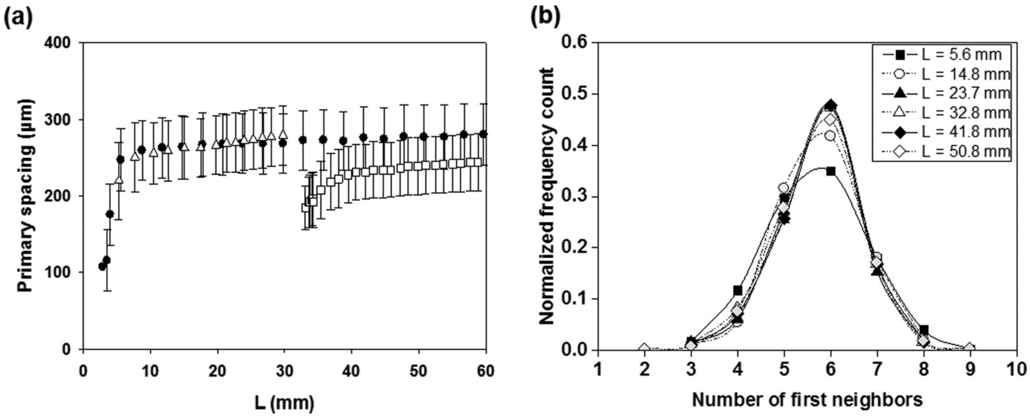

FIG. 2. (a) Evolution of the primary spacing (λ) as a function of the pulled length ($L = Vt$) at $G_1 = 19\,\mathrm{K/cm}$. Primary spacings for the same pulling velocity are compared ($V = 1\,\mu\mathrm{m/s}$) for different experimental situations. ●: long solidification at constant pulling rate; Δ: pulling rate jump from $V_1 = 1\,\mu\mathrm{m/s}$ to $V_2 = 8\,\mu\mathrm{m/s}$ after 30 mm; □: pulling rate jump from $V_1 = 8\,\mu\mathrm{m/s}$ to $V_2 = 1\,\mu\mathrm{m/s}$ after 30 mm. For experiments with pulling rate jumps, only the data corresponding to the part at $V = 1\,\mu\mathrm{m/s}$ are represented. (b) Distribution of the number of nearest neighbors at different times (or pulled lengths) for the long solidification at constant pulling rate $V = 1\,\mu\mathrm{m/s}$, $G_1 = 19\,\mathrm{K/cm}$ [symbol ● in (a)].

grey level below threshold may disappear on the binary image [e.g., "DC" (dark cell) in Fig. 1(b)]. Other defects also appear in this binary image, mainly coming from (i) bright flat parts at groove bottoms (GBs), and (ii) ongoing tip-splitting (TS) events. Corrections are performed to remove the small objects due to bright grooves, tip-splitting events, and details attached to bright area boundaries, to fully disconnect the bright areas associated with each cell [Fig. 1(c)]. The superimposition of the contours of apparent cell surfaces after the processing of the initial image is given in Fig. 1(d). Every single cell is then tagged [Fig. 1(e)], the position of its center determined, and its area measured. The same processing is then applied to all images in the sequence. We keep the same tag number for each cell over the entire sequence of images. Even if the acquisition frequency is higher, only one image/min is sufficient for an efficient analysis. This process is implemented over the whole sequence to get apparent cell area variation with time.

For a given cell i at a given time t, the apparent area $A_i(t)$ can be normalized between its maximum ($A_{i,\,\max}$) and minimum ($A_{i,\,\min}$) values as

$$\tilde{A}_i = \frac{A_i(t) - A_{i,\,\min}}{A_{i,\,\max} - A_{i,\,\min}}. \tag{1}$$

The surface area $A_i(t)$ of each cell can be fitted to a periodic function $f_i(t) = B_i + C_i \sin(\frac{2\pi t}{\tau_i} + \varphi_i)$ for which B_i and C_i as well as the oscillation period τ_i and the initial phase φ_i are fitting parameters. We can thus extract the individual instantaneous phases $\theta_i(t) = \frac{2\pi t}{\tau_i} + \varphi_i$ for all the cells. Considering that experimental curves are quite noisy, fits have to be performed on at least two periods. Even for these relatively short durations, the measured transient oscillation phases may exhibit variations with respect to fitted curves. Thus, fitted data correspond to a moving average over the fitting duration rather than exactly instantaneous values. The normalized oscillation amplitude corresponds to the ratio between the oscillation amplitude and the average surface value, namely the ratio C_i/B_i.

III. RESULTS

A. Pattern selection and oscillation characteristics

1. Pattern spatial ordering

Before describing the oscillation features, it is important to briefly underline the typical characteristics of the extended 2D cellular patterns grown in the range of control parameters for which oscillation appears. As a representative example, let us focus on an experiment of about 60 mm of solidification, starting from rest, at the constant pulling rate of $1\,\mu\mathrm{m/s}$ and thermal gradient $G_1 = 19\,\mathrm{K/cm}$. The primary spacing (λ) evolution with time or, equivalently, with pulled length ($L = Vt$), is given in Fig. 2(a) (black disks). The data points correspond to an average through the entire cellular pattern; the vertical bars correspond to the standard deviation of the spacing distribution. The primary spacing increases until it reaches a steady-state value. An image of the steady-state pattern is given in Fig. 3(a): the ring-shaped fast Fourier transform (FFT) in the inset highlights the high spatial disorder of this array. The time evolution of disorder is illustrated in Fig. 2(b) by the evolution of the distribution of the number of nearest neighbors. A perfect hexagonal tiling would correspond to six nearest neighbors for each cell. The distributions of Fig. 2(b) stabilize after roughly 20 mm of growth, with a high number of topological defects that are mainly instances of five and seven nearest neighbors. The area marked with a white square in Fig. 3(a) is enlarged in Fig. 3(b) at three different times (1.5, 6.7, and 14.1 h after the beginning of solidification) and the number of first neighbors is shown for each cell. Comparing the two first images confirms the decrease of disorder between transient and steady state. The comparison of the last two images reveals that, in spite of a similar global distribution of number of nearest neighbors, the local topology of the pattern still evolves, indicating permanent array dynamics. Such disordered hexagonal arrays are typical from solidified cellular patterns [42]. Even if the cubic symmetry of the interfacial energy anisotropy affects the stability of the pattern [34], in the cellular regime, cell shape does not reflect the

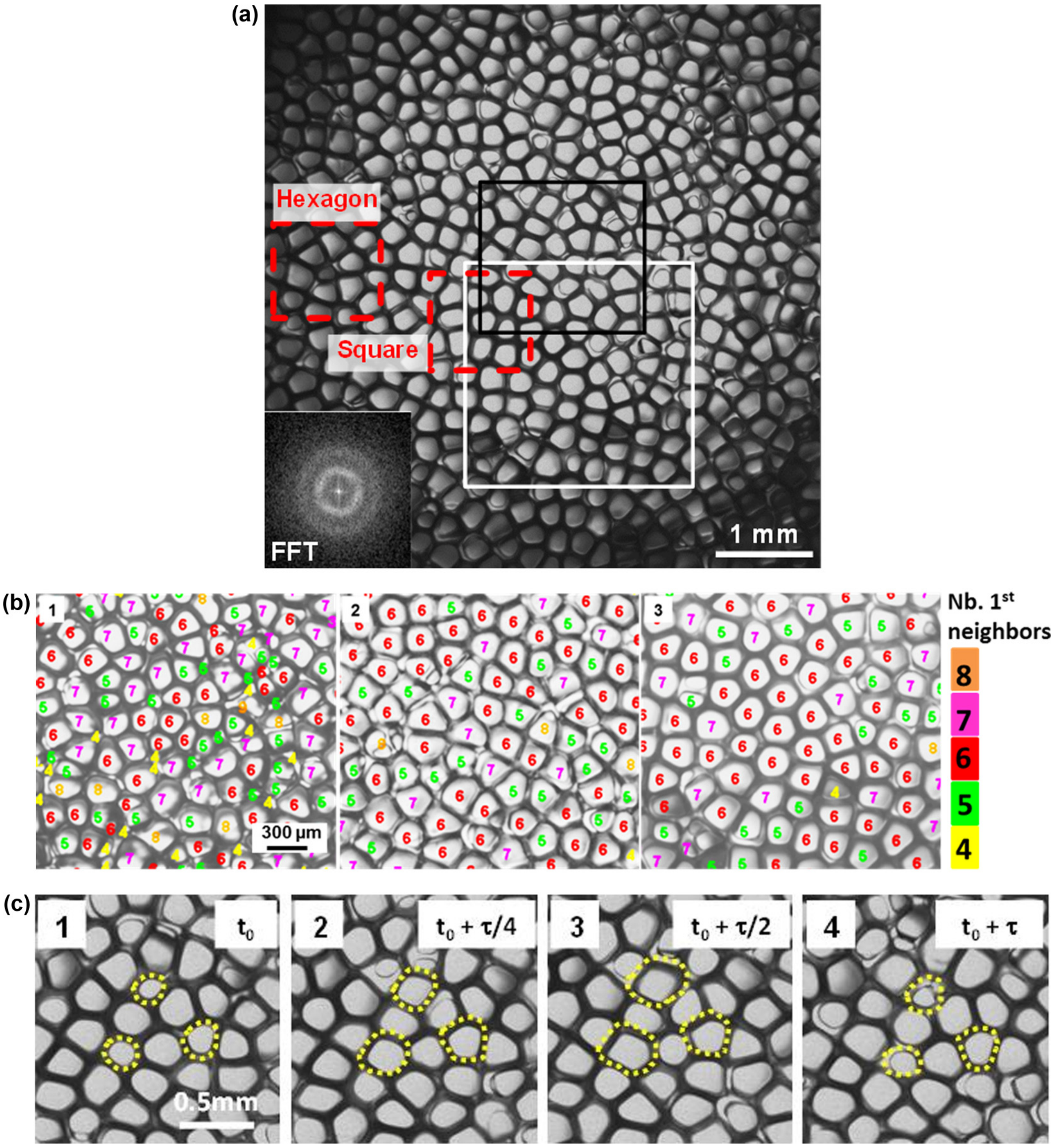

FIG. 3. (a) Global view of the interface at $t = 13.9\,\mathrm{h}$ ($L = 50\,\mathrm{mm}$), for $V = 1\,\mu\mathrm{m/s}$ and $G_1 = 19\,\mathrm{K/cm}$, with the corresponding FFT image highlighting the high spatial array disorder. (b) Enlarged view of first neighbors in the area marked with a white square in (a) at different times: 1.5 h (5.4 mm), 6.7 h (24.1 mm), and 14.1 h (50.8 mm). (c) Enlarged view of area marked with a black square in (a) at different times $t_0 = 14.3\,\mathrm{h}$, $t_0 + \tau/4 = 14.6\,\mathrm{h}$, $t_0 + \tau/4 = 14.8\,\mathrm{h}$, and $t_0 + \tau = 15.1\,\mathrm{h}$ (oscillation period $\tau = 48$ min).

crystal anisotropy and the overall spatial ordering corresponds to the natural hexagonal structure of an isotropic self-similar space filling structure. Defects originate in the first stages of pattern formation and in interactions of the pattern with subboundaries, crucible boundary, or other defects; a high pattern dynamics contributes to maintain the disorder. Similar behaviors can be found in other typical hexagonal patterns, as for example in Bénard-Marangoni convection [43].

2. *Oscillatory behavior*

Oscillating cells are characterized by a periodic variation of the apparent surface area of each cell (see the Supplemental Material for videos [41]). The experiment in Fig. 3(a), started from rest at $V = 1\,\mu\mathrm{m/s}$ and $G_1 = 19\,\mathrm{K/cm}$, is the most illustrative one: oscillation starts during transient, affects the whole pattern, and is sustained during the entire solidification. It will therefore be used as a representative reference and many characterizations will be performed on this experiment. In these conditions, each cell in the whole cellular pattern oscillates. The central area marked with a black square in Fig. 3(a) is enlarged in Fig. 3(c). In the four-image sequence, three different cells are marked with yellow dotted lines to illustrate the variation of their apparent cell surface as a function of time. Since the center-to-center distances (primary spacing) remain constant, grooves between cells oscillate laterally. Cell surface areas increase and decrease periodically. In Fig. 3(c), τ represents the oscillation period.

The oscillation periods for all oscillating patterns measured in our experiments are gathered in Table I. Measurements

TABLE I. Experimental conditions (thermal gradient G, pulling velocity V) for which oscillating patterns were observed, and corresponding period of oscillation τ. The last two lines correspond to experiments with pulling rate jumps from V_1 to V_2 performed after 30 mm of pulling; solidification was then continued for 30 mm at V_2.

G (K/cm)	V (μm/s)	τ (min)
19	0.5	124 ± 7
19	0.75	76 ± 12
19	1	48 ± 2
19	1.5	26 ± 3
12	0.5	160 ± 22
19	$V_1 = 1$ (oscillating) $\rightarrow$ $V_2 = 8$ (nonoscillating)	44 ± 4
19	$V_1 = 0.35$ (planar front growth) $\rightarrow$ $V_2 = 0.75$ (oscillating)	76 ± 5

show that the oscillation period τ is remarkably uniform throughout the entire array, in agreement with spatially extended phase-field simulations [36]. Previous phase-field simulations also revealed that this period seems unaffected by the spatial disorder of the pattern so that it depends only on the experimental control parameters. Additional simulations presented later in Sec. III B 3 (Fig. 12) also show that the oscillation period depends predominantly upon the growth velocity.

The oscillation periods found for extended 3D samples are one order of magnitude higher than those found in thin samples ($1 < \tau < 10$ min) [28], which is expected from the differences of experimental control parameters. In both cases, however, the period is significantly larger than the solutal diffusion time τ_d as $\tau/\tau_d > 7$ in our case and $\tau/\tau_d > 4$ for confined samples ($\tau_d = D/V^2$, where D is the solute diffusion coefficient in the liquid equal to 270 $\mu m^2/s$). Oscillation has been observed for only one pulling rate at $G_2 = 12$ K/cm, all the other measured points being at $G_1 = 19$ K/cm, so that it is not possible to analyze the dependency of the period with the thermal gradient. The experimental period as a function of the pulling rate is represented in Fig. 4; it can be fitted by the power law $\tau = 2.8 \times 10^3\ V^{-1.5}$, with τ in seconds and V in μm/s, for $G_1 = 19$ K/cm. Despite the different alloys and geometries, the exponent and prefactor obtained are both similar to those found in breathing modes in thin samples [28]. In thin samples, the confinement imposes cells to arrange in a row. Yet, for a sample thickness above ≈25 μm, tip shapes are no longer ribbonlike (2D) but actually 3D [12], meaning that thin samples are not exactly 2D but rather represent a "confined-3D" configuration. The Péclet number ($\mathrm{Pe} = \lambda V/D$) is used to compare the cell size (λ) to the solutal length (D/V). In both thin and 3D samples, interactions are limited to first neighbors since Pe ≈1 ($0.5 < \mathrm{Pe} < 1.5$ in our experiments). This probably justifies the similar power law exponent. A possible interpretation for the agreement on the prefactor could be attributed to the nature of the solvent (succinonitrile in both cases). Since experimental data for other alloys is not available, it is currently not possible to check this interpretation.

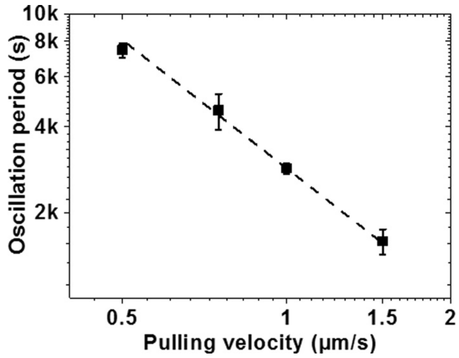

FIG. 4. Oscillation period τ as a function of pulling velocity V ($G_1 = 19$ K/cm): ■, experimental; - -, fit by the power law $t = 2.8 \times 10^3\ V^{-1.5}$, with τ in s and V in μm/s.

3. *Local oscillation coherence*

Examples of surface area measurements as a function of time, for $V = 1$ μm/s and $G_1 = 19$ K/cm, are given in Fig. 5 that illustrate different possible regimes of oscillation and synchronization among neighboring cells. The coexistence of these different kinds of oscillation modes leads to complex dynamics in the 3D samples. In Fig. 5(a), we can see a "standard" oscillation, adopted by many cells on long duration, which corresponds to a periodic and regular oscillation of the cell area between its minimal and maximal values. The average area remains constant, as do the oscillation period and phase value. In Fig. 5(b) an example is given of oscillation with tip-splitting events occurring in the course of cell oscillation. Two types of tip-splitting events are illustrated. The first type, following the circles (●) in Fig. 5(b), is illustrated in Figs. 6(a)–6(d) (at about $t = 7$ h of growth): the parent cell [● of Fig. 5(b)] splits into two represented by squares (■ and □), the full one dominates (■) and oversteps the empty one, and oscillation resumes unaffected. The second type, following the squares (■) in Fig. 5(b), is shown in Figs. 6(e) and 6(f) (at $t = 10$ h of growth): after splitting, the two new cells survive and enlarge; they oscillate with the same phase at the beginning as a doublet element in the array until they decouple and insert as separate elements in the array, which is marked by phase shifting. An example of phase shifting not associated to tip splitting, but rather to a change of neighbor synchronization, is given in Fig. 5(c). The cells marked with triangle (▲) and circle (●) oscillate with their own phases, while the cell noted with diamond (♦) first oscillates in phase with the circles (●) and then shifts to oscillate in phase with the triangles (▲).

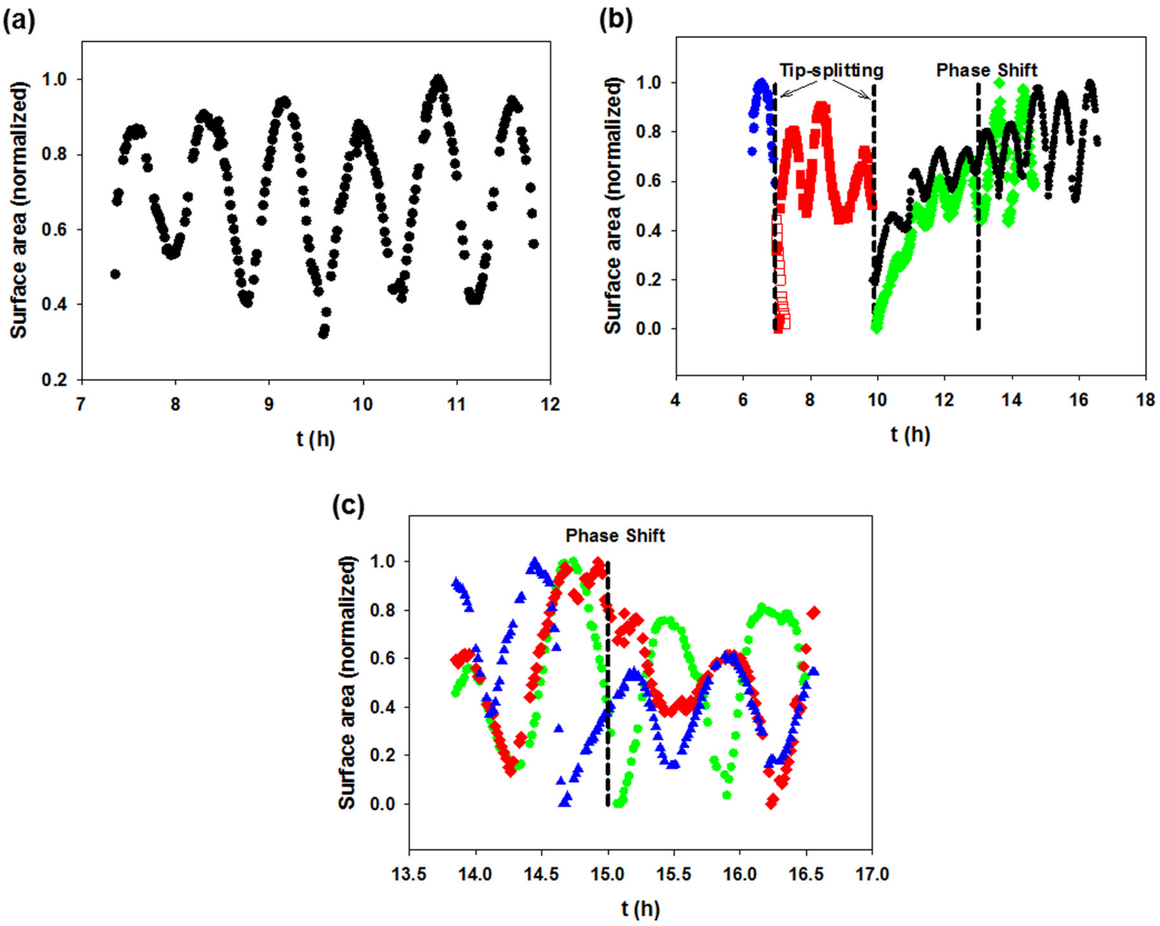

FIG. 5. Different oscillation behaviors observed experimentally for $V = 1\,\mu\text{m/s}$ and $G_1 = 19\,\text{K/cm}$ started from rest. (a) Standard oscillation. (b) Oscillation with tip-splitting events: the first tip splitting of the parent cell (●) around 7 h leads to two cells (■ and □) among which only one survives (■); this cell is also subject to a tip splitting after about 10 h, and the two cells survive, oscillate in phase for some time before ● shifts out of phase and is eventually eliminated. (c) Oscillation with phase shift: the cell marked with ♦ is initially in phase with ● before shifting its phase to synchronize with ▲.

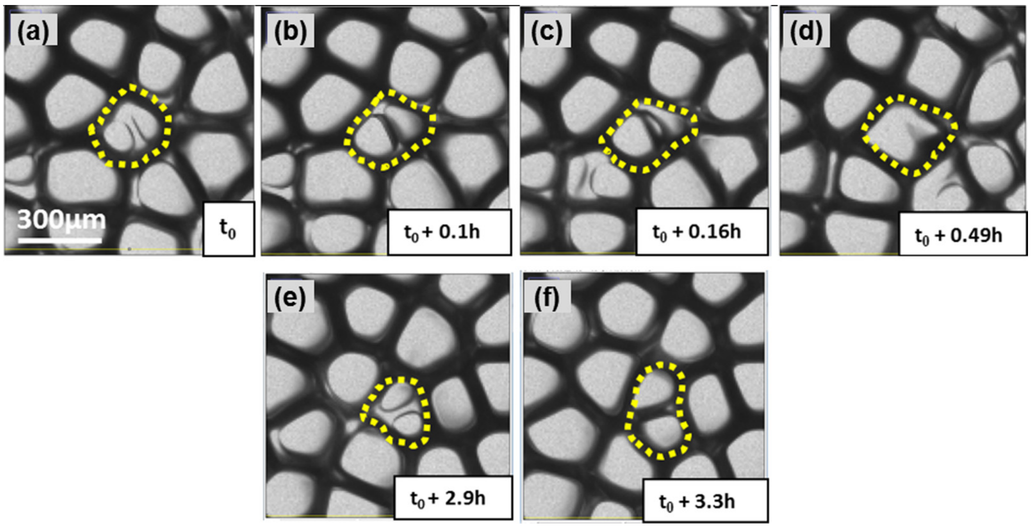

FIG. 6. Examples of characteristic tip-splitting events: (a)–(d) tip splitting with overgrowth of one of the “daughter” cells by its “sister”; (e),(f) tip splitting where the two “daughters” survive and grow ($t_0 = 6.89\,\text{h}$, $V = 1\,\mu\text{m/s}$ and $G_1 = 19\,\text{K/cm}$).

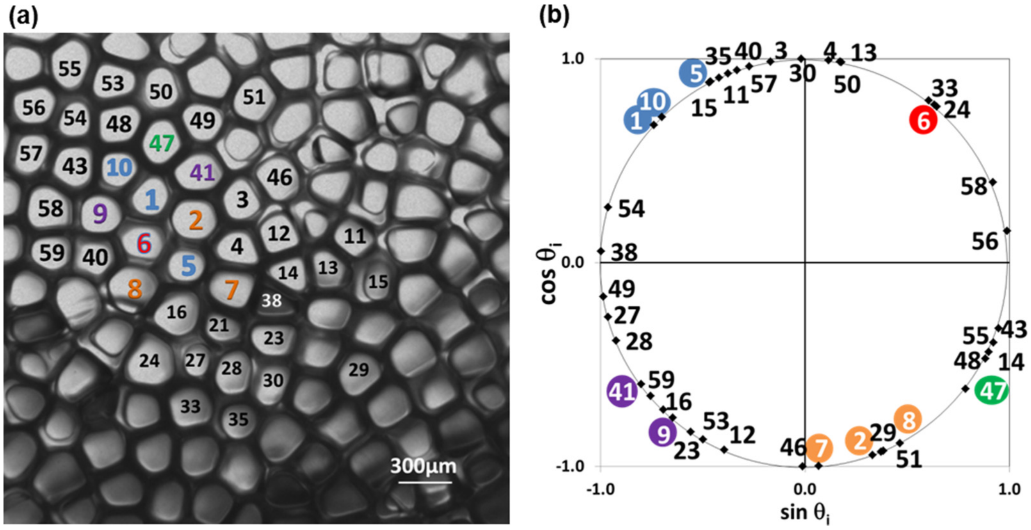

FIG. 7. (a) Enlargement of the square area with white border of Fig. 3(a). Some cells are tagged to identify their instantaneous phases on the unit circle presented in (b); the same color of tag denotes that phases are close ($L = 56\,\mathrm{mm}$, $t = 15\,\mathrm{h}$, $V = 1\,\mu\mathrm{m/s}$, $G_1 = 19\,\mathrm{K/cm}$).

During the process of phase shift, no change of first neighbor is observed for the cell noted with diamonds (♦).

One of the striking features of the 1D oscillating patterns reported by Georgelin and Pocheau [28] is the systematic phase opposition observed between adjacent cells, implying a long-range spatiotemporal coherence. The situation is significantly different in our 2D patterns that exhibit a high level of topological disorder. Similarly, Perrut *et al.* [35] report the observation of a spatially incoherent mode of oscillation in disordered rodlike eutectic pattern; no coherent oscillation mode was found. The existence of long-range coherence may thus be attributed to the forced spatial ordering of cells in a 1D row in thin sample experiments. Yet, even if the patterns in our experiments do not display long range order, small areas presenting a square or a hexagonal local arrangement may exhibit local oscillation coherence, as exemplified by regions marked by the dashed red lines in Fig. 3(a). Their size, however, is always limited to a few cells. Next, we examine the spatiotemporal coherence of the oscillation, in relation to the characteristics of the pattern order.

The surface areas $A_i(t)$ of each cell in the white-bordered square region of Fig. 3(a), enlarged in Fig. 7(a), have been analyzed to extract the individual instantaneous phases $\theta_i(t) = \frac{2\pi t}{\tau_i} + \varphi_i$, as described in Sec. II C. About 50 of these pseudoinstantaneous phases are plotted on the unit circle [Fig. 7(b)] for a solidification time of $t = 15\,\mathrm{h}$ ($V = 1\,\mu\mathrm{m/s}$; $G_1 = 19\,\mathrm{K/cm}$). If we extend the analysis to include about 350 cells, the unit circle is randomly filled. This large scatter of phases on the circle indicates the absence of global oscillation coherence. Moreover, adjacent cells do not present systematic phase relation. To illustrate this, we focus on the group of cells labeled in color in Fig. 7(a), and identified by their numbers on the unit circle of Fig. 7(b). Let us consider the cell 1 and see its phase relations with its neighbors: cell 1 oscillates in phase with 10, in phase opposition with 47, in quadrature of phase with 6 and 9, in nearly quadrature of phase (77°) with 41, and with a phase difference of 150° with 2. This lack of coherence is related to the intrinsic lack of order of the extended patterns comparable to liquid structures with numerous topological defects. Phase-field simulations have shown that, if no specific order is imposed, the pattern displays the same spatial disorder and lack of oscillation coherence as in experiments, whereas long-range coherence sustained for long duration over the entire array may be obtained when starting from a perfect hexagonal arrangement, or enforcing a perfect hexagonal pattern [26,36].

Experimentally, we observed the synchronization of neighboring cells in a few areas where local spatial ordering was maintained long enough. For example, cells 1–7 of Fig. 8(a) display a hexagonal order. The variation of their apparent areas reveals three groups of cells (1-2-3, 4-5-6, and 7) organized as three subarrays that oscillate with the same period, with all the cells of the same subarray oscillating in phase (Fig. 9). Phase shifts between the three subpatterns are of the order of ±120°, as seen in Fig. 8(b), where the surface area of one cell of each group is represented as a function of time. In spite of its local character, this configuration is similar to the synchronization observed in the numerical simulations starting from a perfect hexagonal array, thus confirming that coherence directly results from the hexagonal ordering [26,36]. A qualitatively similar hexagonal mode was found in earlier numerical studies, albeit in the high velocity limit or with a two-sided phase field model [34]. Considering the equivalence of the three subarrays in the oscillation, phase shifts between the three subarrays of cells are expected to be ±120° but measurements reveal that phase shifts are somewhat different from these ideal values, even if this does not modify the fundamental dynamics of the three subarrays. In Fig. 9, cells 1–3 oscillate in phase; 4–6 also oscillate in phase but with a ≈149° phase shift with respect to the first group; while the central cell 7 oscillates with a ≈−130° phase shift with respect to the first group. The origin of the departure of phase shifts from the ideal value of 120° is in part disorder. In a perfect hexagonal tiling, one would expect by symmetry

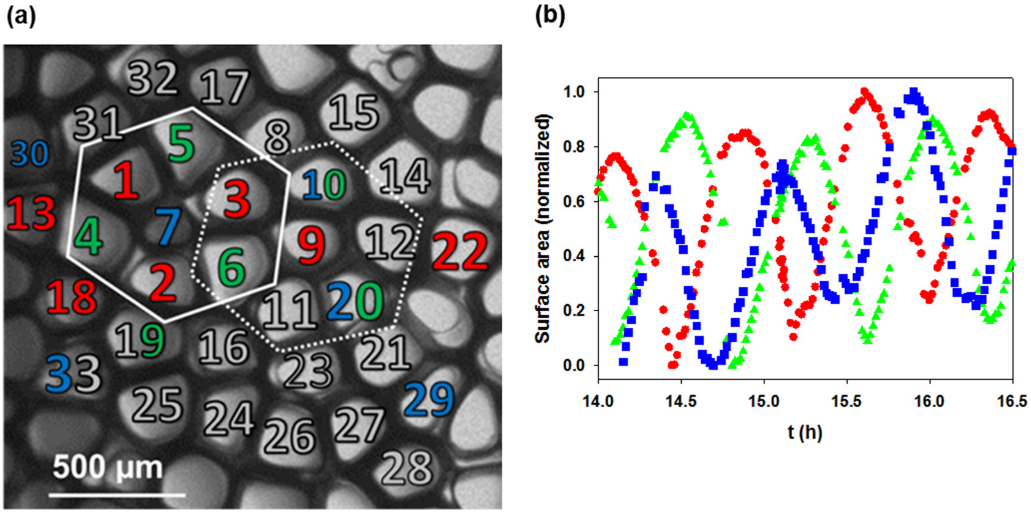

FIG. 8. (a) Interface area presenting a locally hexagonal order formed by cells 1–7. (b) Apparent areas of cells of the three subarrays distinguished in the hexagonal structure formed by cells 1–7 (●, cell 3; ▲, cell 4; and ■, cell 7) ($L = 56$ mm, $t = 16$ h, $V = 1\ \mu$m/s, $G_1 = 19$ K/cm).

that each cell would play the same role in the oscillations, thus exhibiting similar oscillations periods and amplitudes. In practice, disorder induces local variations of primary spacing, making this ideal situation out of reach. Moreover, previous phase-field simulations have shown that perfect hexagonal patterns also exhibit a second oscillation mode of longer period that affects the oscillation amplitudes and phase shifts between the three subarrays [36]. The phase shifts among the three groups of cells oscillate around 120° with a much longer period (e.g., with a period of about 7 h for $V = 1\ \mu$m/s and $G = 13$ K/cm in Fig. 13 of Ref. [36]). The fact that this secondary oscillation requires a sustained perfect hexagonal pattern over a long time prevents its observation in the current experiments. The relative importance of topological disorder and of this long oscillation mode is difficult to evaluate, as experimental patterns are far from perfectly hexagonal; however, these two elements offer an explanation for measured phase shifts differing from ±120°.

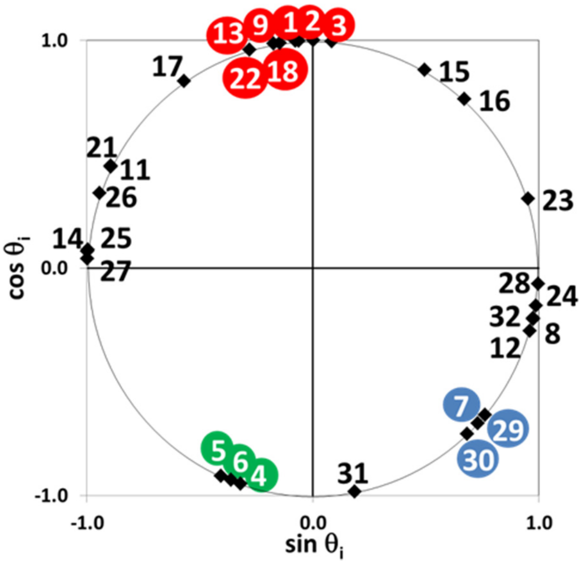

FIG. 9. Instantaneous phases of the cells tagged in Fig. 8(a) reported on the unit circle ($t = 16$ h, $V = 1\ \mu$m/s, $G_1 = 19$ K/cm). The same tag color indicates that cells oscillate in phase.

A detailed analysis of the surrounding area of these locally ordered patterns shows that this coherence is limited to first neighbors, as illustrated in Fig. 8(a): cells that are in phase with one of the three groups of the hexagon are tagged with the same color, phase shifts from one to another of these two groups are identified by bicolored numbers, all grey tags correspond to other values of phases. Most of the cells surrounding the hexagon formed by cells 1–7 have phases tagged in grey, corresponding to none of the three subarrays of the hexagon. The coherence does not extend to the hexagon formed by cells 3, 6, 9, 10, 11, 12, and 20 (dotted lines) even if some cells are shared. For instance, since cell 9 is adjacent to cells 3 and 6, it should be in phase with cell 7 which is not the case: it oscillates in phase with 1, 2, and 3. The instantaneous phases of these cells, placed on the unit circle in Fig. 9, show that coherence is lost beyond first neighbors.

Another example of synchronization is illustrated in Fig. 10, this time in a square pattern: cells 10, 54, and 57 of Fig. 10(a) oscillate together, in phase opposition with the other group (43, 48, 55, 56). The surface area of one cell of each group is represented as a function of time in Fig. 10(b). In the extended 2D patterns where the natural underlying order is mainly hexagonal, we can attribute the appearance of square order to the particular coupling between cells and grain subboundaries that occurs during the first stages of cellular pattern formation. Groups of cells in contact with a grain subboundary arrange themselves perpendicularly to this subboundary, so that at this stage, many cells situated on one side of the subboundary are facing a cell on the other side, like in a square tiling [44]. Such an organization along subboundaries can be seen for example in Fig. 10(c).

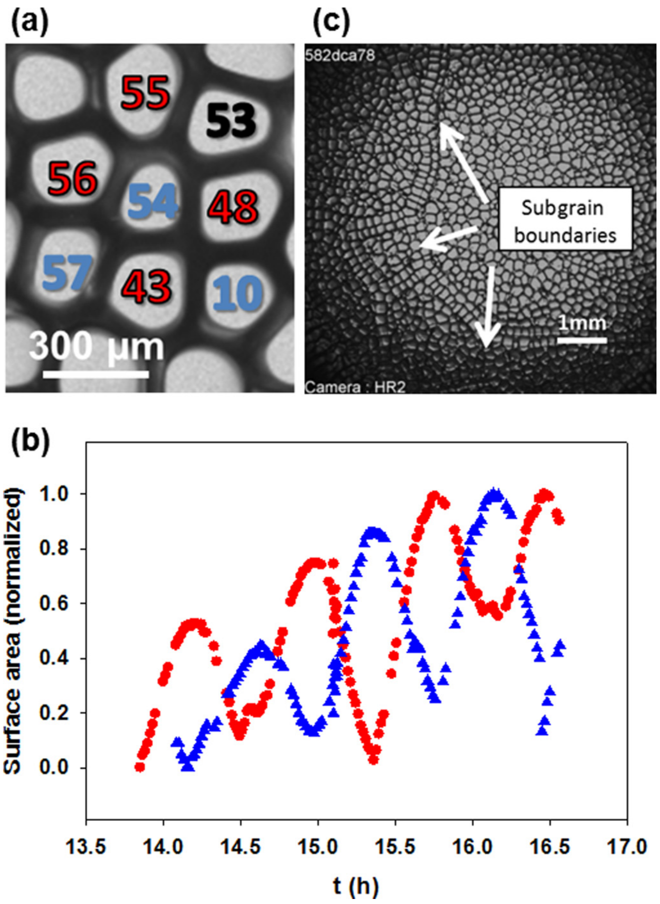

FIG. 10. (a) Oscillation in a regular square structure for $V = 1\,\mu\text{m/s}$ and $G_1 = 19\,\text{K/cm}$. (b) Cells 43, 48, 55, and 56 oscillate in phase; as do cells 10, 54, and 57; and the two groups oscillate in phase opposition as illustrated by the apparent surface areas as a function of time for one cell of each subarray (●, cell 54; ▲, cell 43). (c) Top view of the interface at $t = 2.3$ h (8.3 mm) where the subboundaries are visible with cells arranged perpendicular to them.

B. Occurrence and inhibition of oscillation

1. *Parameter range of occurrence*

The oscillation mode was observed in a narrow range of pulling rates: from 0.5 to 1.5 μm/s for $G_1 = 19\,\text{K/cm}$, and at 0.5 μm/s for $G_2 = 12\,\text{K/cm}$. This range is relatively close to the critical velocity V_c, corresponding to the transition from planar to cellular fronts, which is equal to 0.25 μm/s for G_1, and 0.16 μm/s for G_2 [40,45]. The oscillation modes are bounded in the velocity range $2 < V/V_c < 6$, which is in good agreement with the results obtained for thin samples at $V/V_c \approx 4.5$ [28].

Oscillation is not always observed during the entire experiment. The entry named “Oscillation start” of Table II characterizes the beginning of noticeable oscillation, which always occurs during the initial transient while the interface velocity increases. Using the side-view observation of the interface and analyzing the interface motion [40], it is possible to estimate the corresponding instantaneous interface velocity (V_i). The range of primary spacing measured at this time is also given. (The drift velocity V_d data in each column, as well as the second table entry, “Oscillation stop in the left side,” are explained and discussed later.) The last entry, “Oscillation end,” indicates whether oscillation continues until the end of the experiment (label “end” in column L) or ceases while pulling, in which case the value in column L indicates the solidified length at which oscillation stops; interface velocity V_i and primary spacing λ are also given. In the following subsections, we discuss conditions and events that either promote or inhibit those transient or sustained oscillatory modes. (Thus, additional entries in Table II are discussed in further detail in Sec. III B 4, pertaining to oscillation inhibition by pattern drift.)

2. *Link to tip-splitting events*

In the thin sample experiments of Georgelin and Pocheau [28], tip splitting or disappearance by overgrowth inhibited oscillation: two adjacent cells of an overgrown cell tended to restabilize in a doublet structure and tip-splitted cells also turned to stable doublet structures, leading to the conclusion that phase defects inhibit the oscillatory instability. This behavior is not observed in our extended 2D pattern for which the spatial reorganization is strong and the associated phase shifting is regularly observed, and where local doublets are not stable (see Fig. 5 and its discussion in Sec. III A 3). Multiplet growth modes were observed in the DECLIC-DSI, but not in the range of control parameters yielding cell oscillations.

3. *Link to individual cell stability*

Previous phase-field simulations have shown that oscillatory modes of cells in a hexagonal arrangement occur for narrow ranges of primary spacings close to the limits of stability of individual cells [26,36]. Depending on control parameters, the stable spacing branch can be continuous or exhibit a stable spacing gap. Similarly as described in [36], we calculated the stability range for a single cell in a hexagonal pattern for pulling velocities $V = 1.0$ and 1.5 μm/s and various temperature gradients, using the recently reassessed solute partition coefficient for succinonitrile - 0.24 wt % camphor, $k = 0.07$ [45]. Other parameters of the phase-field simulations are liquid solute diffusion coefficient $D = 270\,\mu\text{m}^2/\text{s}$; interface Gibbs-Thomson coefficient $\Gamma = 6.478 \times 10^{-8}\,\text{K m}$; liquidus slope $m_L = -1.365\,\text{K/wt}\,\%$ camphor; surface tension anisotropy $\varepsilon_4 = 0.011$. The finite difference grid spacing $\Delta x/W = 1.2$, and the diffuse interface width is $W/d_0 = 198$ for $V = 1.0\,\mu\text{m/s}$ and 160 for 1.5 μm/s, with $d_0 = \Gamma/[m_L C_0(1 - 1/k)]$ the interface solute capillarity length. Further details of simulations procedures are given in [36].

The resulting stability maps for cells in a hexagonal pattern appear in Fig. 11, represented as the stable cell tip undercooling Δ as a function of the primary spacing λ. The opening of the stable spacing gap appears for $G \approx 25\,\text{K/cm}$ for $V = 1.0\,\mu\text{m/s}$ [Fig. 11(a)] and $G \approx 31\,\text{K/cm}$ for $V = 1.5\,\mu\text{m/s}$ [Fig. 11(b)]. This stable λ gap narrows down and ultimately closes when decreasing the temperature gradient, when increasing the growth velocity or for high interfacial anisotropies [20]. As described in [36], oscillations occur toward the high-λ end of the leftmost (low-λ) stable branch, at both limits of the rightmost (high-λ) branch in the case of

TABLE II. Evolution of the characteristics of the oscillating patterns between the onset of oscillation and the end of experiment or oscillation cessation ($G_1 = 19\,\mathrm{K/cm}$). The characteristics may be given for the whole interface or they may refer to specific regions of the interface (left or right), if different behaviors were noted between the two sides of the interface. In that case, oscillation ceases prematurely on the left side for characteristics given in the central column. In the entry "Oscillation end," we refer either to the end of experiment ("end") or to a specific value of pulled length if oscillation ceases before the end of experiment. Oscillation start and stop times are denoted by the pulled length L at which they occur (equivalent to time: $L = Vt$). V_{i} corresponds to the instantaneous interface growth velocity; λ is the primary spacing and V_d is the average drift velocity of the pattern (component of the cell tip growth rate normal to the optical axis). In the last entry, some values are presented in italics because there is no longer oscillation.

	Interface	Oscillation start				Oscillation stop in the left side				Oscillation end			
V (μm/s)	zone	L (mm)	V_i (μm/s)	λ (μm)	V_d (μm/s)	L (mm)	V_i (μm/s)	λ (μm)	V_d (μm/s)	L (mm)	V_i (μm/s)	λ (μm)	V_d (μm/s)
0.5	Whole	9	0.49	259 ± 51	0.008					End	0.50	269 ± 57	0.009
0.75	Left	10	0.74	213 ± 39	0.010	31	0.74	245 ± 44	0.015	End	0.75	*(298 ± 55*	*0.022)*
	Right			206 ± 41	0.004			225 ± 45	0.005			312 ± 49	0.005
1	Whole	6	0.92	225 ± 50	0.007					End	1.00	280 ± 41	0.007
1.5	Left	6	1.44	196 ± 34	0.060	20	1.47	199 ± 34	0.064	30	1.49	*(203 ± 31*	*0.065)*
	Right			204 ± 43	0.017			222 ± 51	0.023			224 ± 42	0.039

existence of a gap, as well as in the immediate vicinity of the stability gap opening.

Thus, we also simulated breathing oscillations of three subarrays of cells in a hexagonal arrangement in the vicinity of the stability gap opening, for set primary spacings and different temperature gradients (see [36] for further details). These simulations are represented with diamond symbols in the insets of Fig. 11, with symbol size representing the oscillations amplitude. Figure 12 summarizes the amplitudes (a) and periods (b) of the resulting breathing oscillations. Figure 12(b) clearly shows that the oscillation period depends only upon the growth velocity V, since variations of a few minutes are of the order of the accuracy on the fitting of the period. Figure 12(a) shows that, in the vicinity of the stability gap, the amplitude of oscillations increases with G, i.e., it increases when getting closer to the gap opening. For a given temperature gradient, the amplitude also decreases when the primary spacing increases. Moreover, as expected from the difference in G at which the stability gap opens, oscillations occur within a lower temperature gradient range for a lower velocity.

The two gray background zones in Fig. 12(a) show amplitudes that do not yield breathing mode oscillations. When the oscillation amplitude is lower than 0.1, the oscillations are essentially noisy, showing little to no synchronization between the three cell groups. On the other hand, when the oscillation amplitude gets higher than 0.8, the oscillations ultimately lead to the elimination of one of the cells. Cell elimination is expected as the amplitude gets closer to 1, since an oscillation of constant amplitude equal to 1 corresponds to the minimum cell area $A_{i,\,\mathrm{min}}$ tending to zero. Therefore, oscillation of cells is expected to yield breathing modes when the oscillation amplitude is between 0.1 and about 0.8.

For the experiment at $1.5\,\mu\mathrm{m/s}$ and $G_1 = 19\,\mathrm{K/cm}$, oscillation ceases before the front reaches the applied pulling velocity. This may be qualitatively understood from the results of Figs. 11 and 12(a). When the velocity increases from 1 to $1.5\,\mu\mathrm{m/s}$, the stability gap opening occurs for higher gradients (Fig. 11) and, for a given gradient, the amplitude of oscillations tends to zero [Fig. 12(a)]. The disappearance of oscillation can then be attributed to the progressive increase of velocity during transient growth. A progressive decrease of the

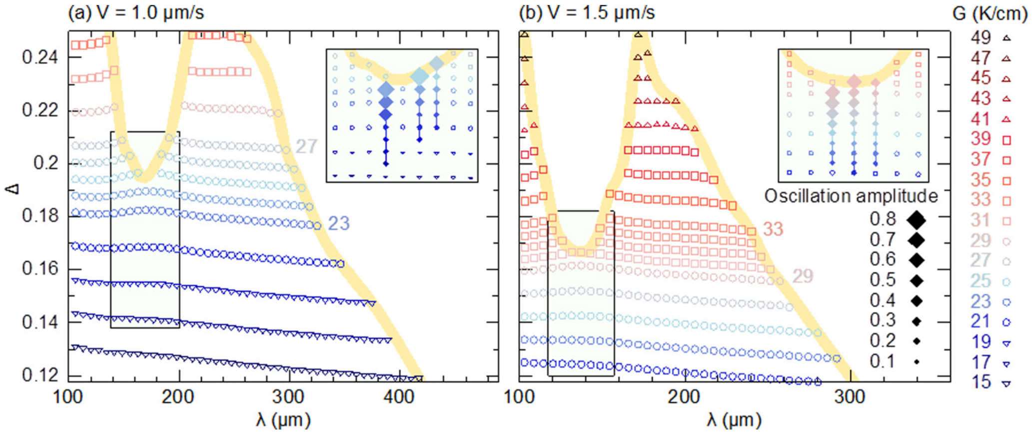

FIG. 11. Stability maps for a quarter of cell in a hexagonal pattern for a pulling velocity $V = 1\,\mu\mathrm{m/s}$ (a) and $1.5\,\mu\mathrm{m/s}$ (b), and different temperature gradients (shown with different colors and symbols, with steps of 2 K/cm, and 1 K/cm in the vicinity of the stability gap), plot as tip undercooling Δ of the stable cells vs primary spacing λ. The thick yellow line is a schematic illustration of the stability limit in the (Λ,Δ) plane. Zoomed-in insets mark configurations explored for oscillatory breathing mode oscillations (Fig. 12).

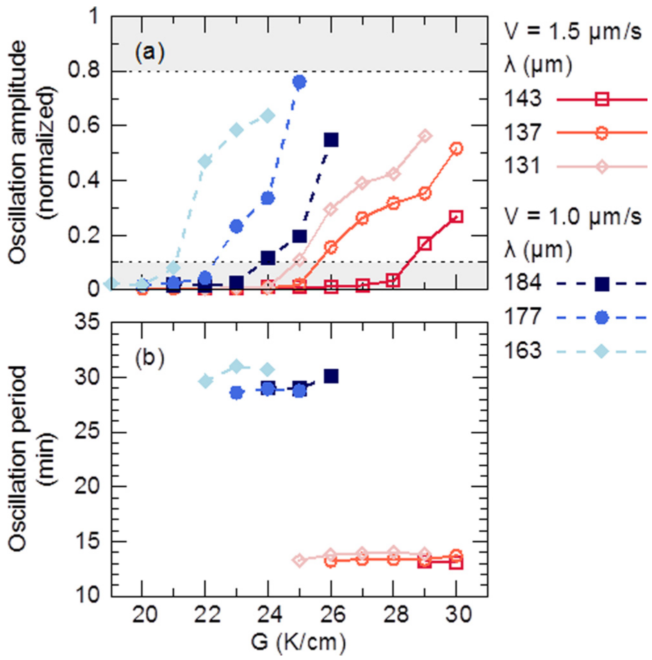

FIG. 12. Breathing mode oscillations amplitude (a) and period (b) vs temperature gradient G for different cases represented in the insets of Fig. 11. Gray background zones in (a) represent noisy oscillations exhibiting no neighbor synchronization for low amplitudes ($\leqslant 0.1$), and configurations unstable with respect to elimination and/or tip splitting for high oscillation amplitudes ($\geqslant 0.8$).

thermal gradient would have a similar effect, but for such very low pulling rates, the impact of latent heat rejection—which is the most evident origin of thermal gradient decrease—is very weak. Furthermore, while oscillations in the current simulations only appear for $G > 21$ K/cm at $V = 1\,\mu$m/s, only small additional uncertainties on material parameters or on the temperature gradient would be sufficient to predict steady oscillations at $V = 1\,\mu$m/s and no oscillations for $V = 1.5\,\mu$m/s for a given temperature gradient (e.g., here for $G \approx 22$ K/cm instead of the estimated experimental value 19 K/cm).

In the experiments, the average primary spacing that marks the onset of oscillation decreases when the interface velocity increases, following the dependence upon V of the spacing stability gap (Fig. 11). For all pulling rates, the range of measured spacings is $\Delta\lambda/\lambda \approx 0.2$ during the whole experiment ($\Delta\lambda$: standard deviation of a primary spacing distribution). In contrast with simulations of perfect hexagonal patterns [Fig. 12(a)], experimental analyses do not reveal a significant dependence of the amplitude of oscillation on primary spacing, as illustrated in Fig. 13(a): the normalized oscillation amplitude is $\approx$0.2 regardless of the spacing ($\approx$250 cells measured at $V = 1\,\mu$m/s). Table II shows that between the onset of oscillation and the end of experiment (or the cessation of oscillation), the average spacing increases from 4 to 50% depending on pulling velocities, the maximum variation of 50% being obtained for the experiment at $V = 0.75\,\mu$m/s. To test the sensitivity of oscillation amplitude to these large primary spacing variations, the amplitudes have been measured in a domain containing about 50 cells during four successive time sequences, corresponding to different distributions of primary spacings [Fig. 14(a)]. In spite of the large increase of the primary spacing, all cells oscillate, and no significant difference of oscillation amplitudes is noticed. A slight decrease of oscillation amplitude can be evidenced by averaging all the data points by primary spacing classes of 10 μm [Fig. 14(b)] but, considering the strong dispersion observed in Fig. 14(a), the slope is too low to be conclusive.

The independence of oscillation amplitude with primary spacing is in sharp contrast with the simulations for perfect hexagonal patterns in Fig. 12(a), clearly showing a decrease of amplitude as the spacing increases. This is an indication that the sustained spatial reorganization in spatially extended samples may contribute to homogenizing the oscillation amplitude throughout the sample. To test this interpretation, we plot in Fig. 13(b) the oscillation amplitudes as a function of the primary spacing for the 51 cells in the spatially extended simulation for $k = 0.21$, $\varepsilon_4 = 0.007$, $V = 1\,\mu$m/s, and $G = 28$ K/cm from [36], which exhibits a wider range of spacings. The width of primary spacing distribution $\Delta\lambda/\lambda$ is similar to the experimental one ($\approx$0.2) and the average

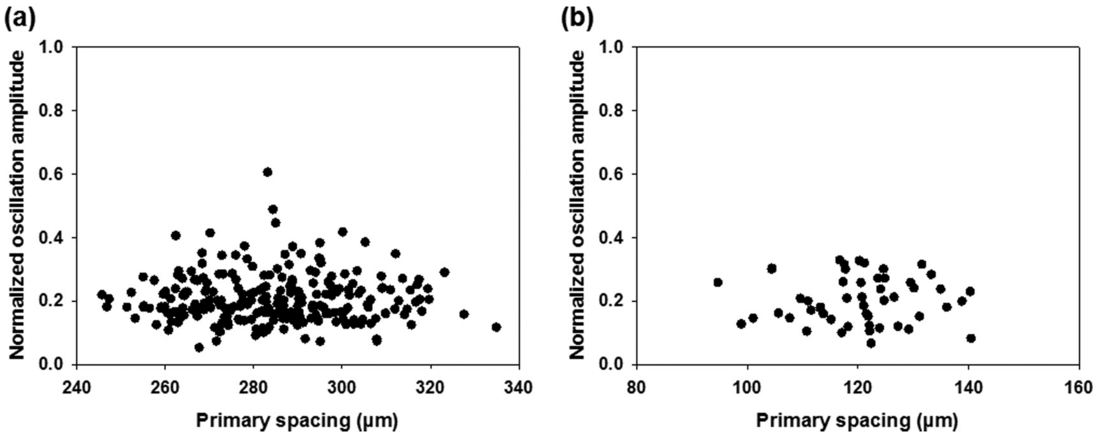

FIG. 13. Distribution of normalized oscillation amplitudes vs individual primary spacing for (a) experimental normalized amplitudes reported for 250 cells (measured between 13.5 and 16.5 h of solidification, $V = 1\,\mu$m/s, $G_1 = 19$ K/cm); (b) 3D phase field simulation for 51 cells between 2 and 10 h of solidification (spatially extended simulation with $k = 0.21$, $\varepsilon_4 = 0.007$, $V = 1\,\mu$m/s, $G = 28$ K/cm [36]).

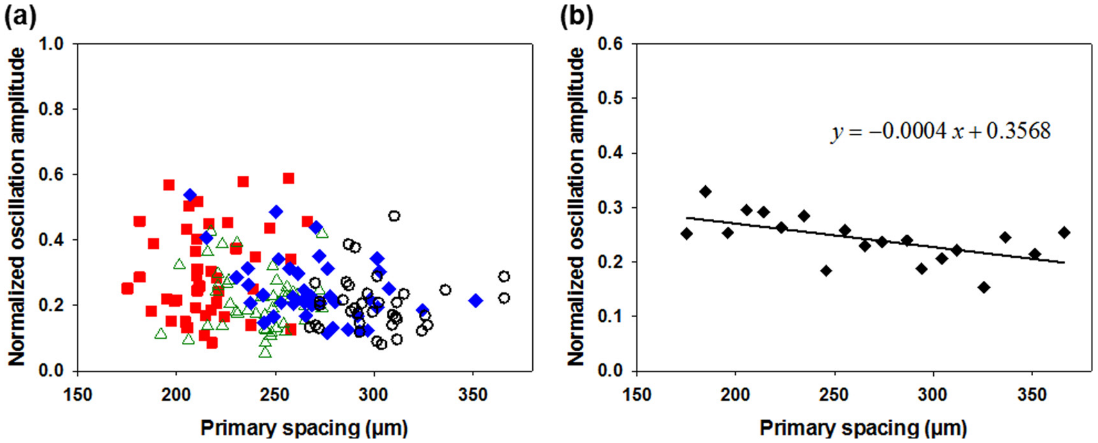

FIG. 14. Long time evolution of the primary spacing observed in the experiment at $V = 0.75\ \mu\text{m/s}$, used to extend the analysis performed in Fig. 13: (a) the experimental normalized oscillation amplitudes as a function of primary spacing are reported for ≈50 cells, for four different time intervals, namely 🟥: 4.1–8.5 h; △: 8.5–13.7 h; ♦: 13.7–16.3 h; ○: 16.3–21.9 h. In (b), all data points are averaged by classes of primary spacing of 10 μm width to evidence the weak dependence of the oscillation amplitude upon primary spacing ($V = 0.75\ \mu\text{m/s}$, $G_1 = 19\ \text{K/cm}$).

of normalized amplitudes of area oscillation is ≈0.2, with no dependence on the spacing, also like in the experiments. Thus, while sustained oscillations in a perfect hexagonal arrangement typically exhibit a variation of oscillation period and amplitude with the primary spacing [Fig. 12(a)], the overall oscillation of cells in a large pattern, accompanied with constant rearrangement of the pattern and evolution of spacings, exhibits little dependence of the oscillation period and amplitude upon the spacing distribution in the sample. It is also interesting to observe that all amplitudes in experiments and in the spatially extended simulation of Fig. 12 show a highest density around an amplitude of 0.2, which was found from Fig. 11(a) to be about the lowest amplitude at which breathing modes may be observed. This may indicate that higher amplitude oscillations in Fig. 14(a) may be metastable, and that the few data points at higher amplitudes in Fig. 13(a) may correspond to transient oscillatory states (e.g., just before or after tip-splitting events).

Additionally, a noteworthy discrepancy between simulations and experiments pertains to selected spacings that are larger in experiment than simulation (see, e.g., Fig. 13). This discrepancy was already pointed out in previous articles [26,36]. It may be due in part to uncertainties on alloy and control parameters (e.g., solute diffusion coefficient, interfacial anisotropy, or temperature gradient). Several of those parameters have thus been reassessed (thermal gradient G [40]) and remeasured (partition coefficient k [45]). However, the revised values have not up to now enabled us to resolve the discrepancy between simulated and observed spacings. It should be noted, however, that the range of experimentally measured spacings at $V = 1\ \mu\text{m/s}$ and $G_1 = 19\ \text{K/cm}$, i.e., from about 240 to 340 μm in Fig. 13(a), falls within the continuous stable branch for hexagonal ordered patterns in Fig. 11(a). Since the simulations to explore the array stability have been carried out for perfectly ordered hexagonal patterns, it is possible that a stable pattern within a larger spacing range encompassing the experimentally observed spacings could develop oscillations in the presence of spatial disorder. Additional factors could be critical in the spacing selection process. The history of the sample, with a pattern stabilizing higher within the spacing stability range due to transient thermal history [40], should be considered, as well as the influence of solid-state solute diffusion. Furthermore, experiments can depart in several aspects from the ideal case of a perfectly oriented and well-ordered single crystal modeled in phase-field simulations. Experiments include imperfections that can help destabilize the solid-liquid interface during the early stages of morphological instability, thereby affecting spacing selection, slight deviations of the $\langle 100\rangle$-growth direction from the pulling direction that induces a drift of the microstructure, or subgrains and concomitant subboundaries, resulting from the polygonization of the initially single crystal seed, which promote square ordering of cellular arrays. Those effects and others could cause dynamically selected cell spacings to be larger in the experiments than the simulations and warrant further investigation. Despite this quantitative discrepancy, current phase-field simulations reproduce the main salient features of the oscillatory modes.

4. Inhibition due to pattern drift

An additional interesting observation, detailed in Table II and observable in videos provided in the Supplemental Material [41], is the fact that the part of the interface affected by oscillation may evolve during pulling. For $V = 1$ and $0.5\ \mu\text{m/s}$, once oscillation starts, it affects the whole interface for the remainder of pulling with all cells oscillating. For $V = 0.75\ \mu\text{m/s}$ [see Supplemental Material [41] and Fig. 15(a)], oscillation initially affects the whole interface but after about 31 mm of pulling (≈11.5 h), cells on the left side of the interface stop oscillating, with characteristics given in the second entry of Table II [labeled “stable region” in Fig. 15(a)], while the oscillation continues on the right side [labeled “oscillating region” in Fig. 15(a)]. The same kind of situation is observed for $V = 1.5\ \mu\text{m/s}$ [see Fig. 16(a)], with oscillation stopping on the left side of the interface after about 20 mm of pulling (≈3.7 h); the complete stop of oscillation, on the right side of the interface, after ≈30 mm

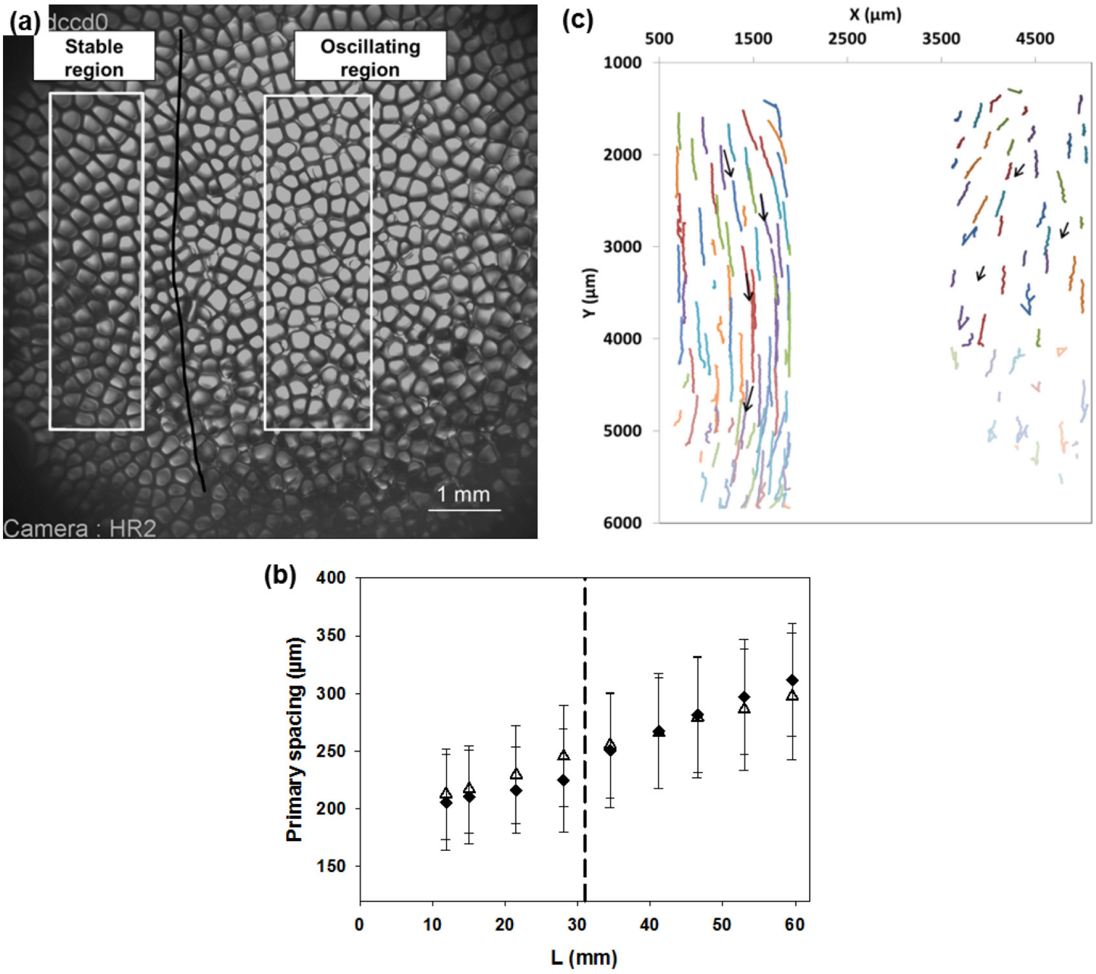

FIG. 15. (a) Top view of the interface during steady-state growth ($t = 15\,\mathrm{h}$; $L = 40.5\,\mathrm{mm}$) for $V = 0.75\,\mu\mathrm{m/s}$ and $G_1 = 19\,\mathrm{K/cm}$. (b) Evolution of the primary spacing as a function of the pulled length (L) for the two regions identified in (a): stable region (Δ); oscillating region (♦). (c) Trajectories of the cells in the boxed areas of (a) between 8.5 h (23 mm) and 16 h (43 mm).

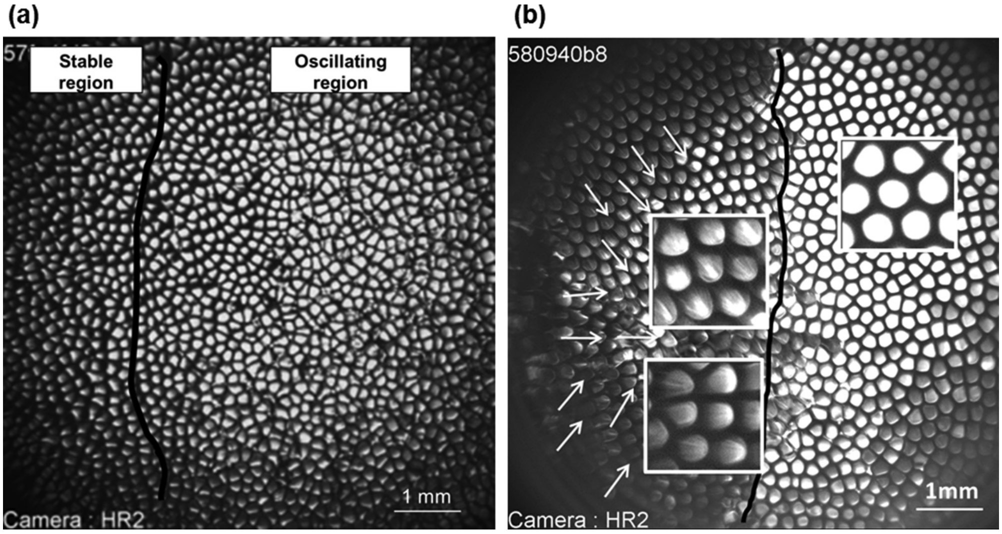

FIG. 16. Top view of the interface at $t = 2.3\,\mathrm{h}$ ($L = 12\,\mathrm{mm}$) (a) and 10.8 h (58 mm) (b), with $V = 1.5\,\mu\mathrm{m/s}$ and $G_1 = 19\,\mathrm{K/cm}$. In (b) the arrows represent the trajectories of the cells followed from 6 to 11 h of solidification (32–59 mm), and three different zones are zoomed 2.5 times to evidence the difference of morphology between the cells of the left side, which are clearly tilted, and the cells of the right side.

of pulling could be attributed to the increase of the growth velocity that reaches the limit of possible oscillating conditions (close to 1.5 μm/s) as previously discussed in Sec. III B 3. In the following paragraphs, we determine the source of early oscillation inhibition on the left part of the interface for the experiments at $V = 0.75$ and 1.5 μm/s.

First, we analyze possible differences of primary spacing in the two regions of the interface. In Fig. 15(b), the primary spacing evolution is characterized in the two interface regions for the experiment at 0.75 μm/s; the dashed line marks the end of the oscillation on the left side. No significant difference appears in the primary spacing distributions between the two interface regions, meaning that the difference of oscillating behavior does not come from primary spacing differences.

The key to understanding the origin of oscillation inhibition in these two experiments is given by the observation of the pattern at $V = 1.5$ μm/s once the microstructure is well developed: in Fig. 16(b), a clear morphological difference is observed between the left region that displays inclined structures and the right region that does not. Inclined structures are due to a misalignment between the preferred growth direction $\langle 100\rangle$ and the pulling (thermal) axis. In practice, the growth direction changes from the thermal gradient direction at low velocity to the closest $\langle 100\rangle$ direction when pulling rate increases [46,47], meaning that the growth direction will be misoriented with respect to the pulling (thermal) axis if no $\langle 100\rangle$ direction is perfectly aligned with this axis. Inclined structures are particularly well revealed by the pattern drift that they induce in the lateral direction (i.e., in the plane normal to the optical axis). Three areas or subgrains are then identified corresponding to different drift directions as indicated by the white arrows in Fig. 16(b). On the other hand, the right side of the interface presents better-oriented structures, which oscillate for long periods of time (i.e., until the front reaches a critical velocity that inhibits oscillations, as discussed before). For $V = 0.75$ μm/s, no obvious microstructural difference is observed between the two interface regions, since the effects of misorientation decrease when the pulling velocity decreases. Trajectories of cells both in the stable and oscillating regions framed in white in Fig. 15(a) are represented for a duration of 7.5 h in Fig. 15(c): a collective drift caused by a misorientation between the crystal $\langle 100\rangle$ and the pulling axis is evidenced in both regions but its amplitude is much higher in the stable region, witnessing a higher drift velocity in this region.

Based on these observations, we systematically characterized the drift in all experiments. The average values of drift velocities are given in Table II. At 0.75 and 1.5 μm/s, the left side of the interface is systematically marked by higher drift velocities as compared to the right side, meaning that the misorientation of the left side is higher than that of the right side. At least one vertical subboundary splits the interface in these experiments, which is not the case for other velocities. Moreover, the drift velocities in the experiments at 0.5 and 1 μm/s are low, comparable to the ones in the right side of the interface of the experiment at 0.75 μm/s. The origin of the subboundaries is not clear: we started the experimental campaign with a single crystal, with a $\langle 100\rangle$ direction aligned with the pulling axis as closely as possible, and only the very top of the solid seed was remelted. We may however suggest dislocation reorganizations into subboundaries, and thus seed crystal polygonization, due to successive thermal cycles, especially considering that the experiments at 0.75 and 1.5 μm/s have been performed near the end of the experimental campaign, several months after the experiments at 0.5 and 1 μm/s.

We now analyze whether the misorientation itself, or the resulting drift, is at the origin of the inhibition of oscillations. If inhibition was directly due to misorientation, transient oscillation in the left part of the interface at $V = 0.75$ and 1.5 μm/s would not occur, as the misorientation is a fixed characteristic of the crystal. A more plausible hypothesis is that the resulting drift inhibits oscillation when a threshold of drift velocity is reached, and that this threshold depends on pulling velocity. Drift and oscillation have their own dynamics, but the oscillation is based on a subtle evolution of the concentration field at the tip of the cell and adding a drift could affect the dynamics of oscillation by modification of this concentration field, and eventually inhibit it if the drift is too important.

On this basis, a direct approach is to compare the dynamics of oscillation and drift. A first criterion can be built by defining the characteristic times of these two phenomena. For oscillation, the natural timescale is the oscillation period τ, and for drift, a characteristic time τ_d can be defined as the time necessary for a cell to glide the most characteristic distance in the array, namely the cell width (or the primary spacing), λ/V_d. In Fig. 17, the ratio τ_d/τ is reported for the different data sets given in Table II. A possible threshold at a ratio $\tau_d/\tau \approx 3$ appears, below which oscillation is inhibited. Below this threshold, the drift velocity becomes too high (i.e., τ_d gets too low), and the drift dynamics disturbs and stops

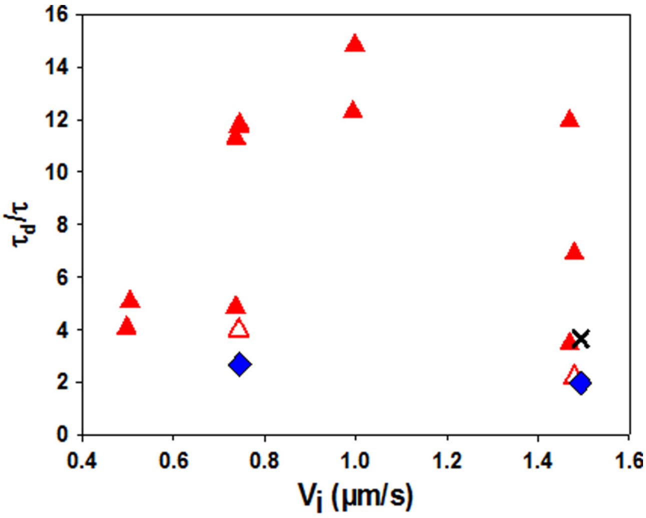

FIG. 17. Ratio of the characteristic times of drift τ_d and oscillation period τ as function of growth rate (V_i), for the different data sets given in Table II: the filled triangles (▲) correspond to oscillating conditions whereas the empty triangles (△) correspond to oscillation inhibition. Diamonds (♦) correspond to nonoscillating conditions, using the oscillating period measured in the same area before the oscillation stops. The cross (x) corresponds to the oscillation stop at $V = 1.5$ μm/s in the right side of the interface, explained by the analysis of the stability gap and its relation to oscillation (cf. Fig. 11) ($G_1 = 19$ K/cm).

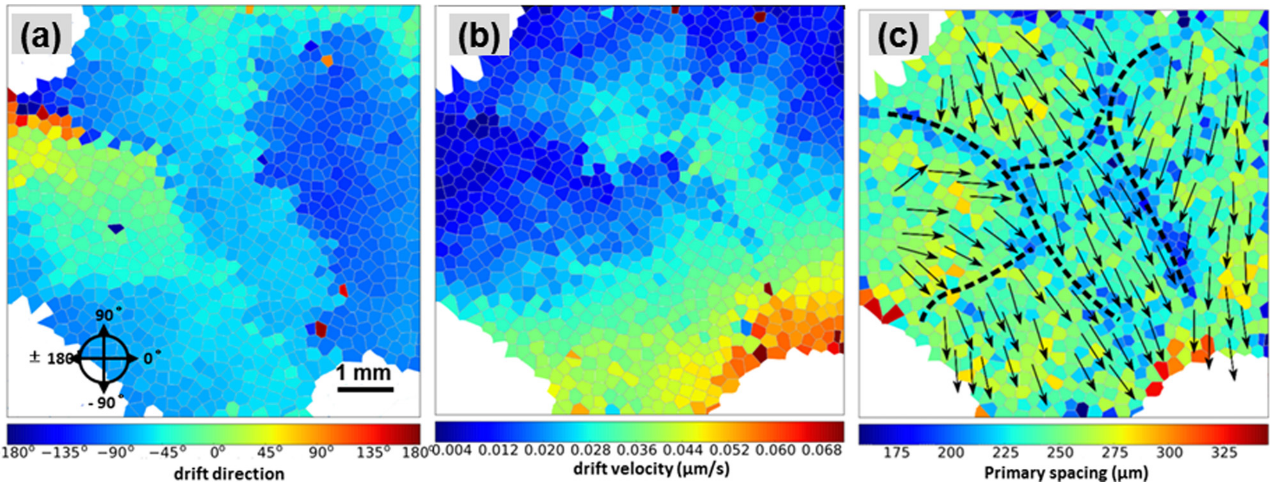

FIG. 18. Analysis of the characteristics of the cells during the growth stage at $V = 1\,\mu\text{m/s}$ after a jump of pulling rate from $V = 8\,\mu\text{m/s}$. Maps of (a) drift direction and (b) drift velocity of each cell, and (c) primary spacing, with dashed lines indicating frontiers between regions of different drift directions, indicated by arrows (length of arrows not proportional to drift velocity). $V = 1\,\mu\text{m/s}$, $G_1 = 19\,\text{K/cm}$, $t = 4.3\,\text{h}$, $L = 41.8\,\text{mm}$ (30 mm at $8\,\mu\text{m/s}$ + 11.8 mm at $1\,\mu\text{m/s}$).

the oscillation dynamics. Another possible criterion can be obtained by considering the oscillation of the growth velocity as reported by Georgelin and Pocheau [28], and comparing the amplitude of the velocity oscillation in the pulling direction to the drift velocity (normal to the pulling): these two components correspond to small deviations from the ideal situation of a stable cell growing parallel to the pulling velocity. For a ratio above unity, oscillation dominates, whereas it is inhibited below unity. Practically, top-view observations do not enable us to measure the amplitude of the velocity oscillation, and side views of the entire pattern do not allow us to isolate such velocities for individual cells. However, if we consider the data reported by Georgelin and Pocheau (Fig. 3 of [28]), the amplitude of oscillation of growth velocity in the pulling direction is of the order of a few percent of the pulling velocity. Considering our values in Table II, we see that the inhibition of oscillation in the left side of the interface for the experiments at 0.75 and $1.5\,\mu\text{m/s}$ occurs respectively for drift velocities equal to 2% and 4.2% of the pulling velocity: such values are very likely comparable with amplitudes of velocity oscillations. Further investigations remain necessary to investigate theoretically and experimentally the effect of drift on the oscillations.

5. *Influence of pulling velocity history*

All the experiments discussed above describe long solidification experiments starting from rest at constant pulling rates, but we also performed experiments with pulling rate jumps after 30 mm of growth, especially starting from or jumping to $V = 1\,\mu\text{m/s}$ ($G_1 = 19\,\text{K/cm}$). Experiments starting from $V = 1\,\mu\text{m/s}$ enabled us to verify the reproducibility of the first half of the long experiment starting from rest, in terms of oscillation characteristics and primary spacing (triangles in Fig. 2).

In the experiments with a different pulling velocity history, starting at $V = 4$ or $8\,\mu\text{m/s}$ and jumping to $1\,\mu\text{m/s}$ after 30 mm of growth, oscillation was not triggered in the $1\,\mu\text{m/s}$ growth stage. Because those two experiments are quite similar, let us focus on the jump from $V = 8\,\mu\text{m/s}$ to $1\,\mu\text{m/s}$. The primary spacing evolution after the jump of velocity is reported on Fig. 2 (square points: the primary spacing evolution during the $8\,\mu\text{m/s}$ growth stage is not shown, explaining that the data starts from $L = 30\,\text{mm}$): the average spacing is smaller than the one obtained in the experiment starting from rest, but the two distributions superimpose on roughly half of their width. In spite of this superposition, no oscillating cell is observed after the jump of pulling rate, even in small areas of larger spacing. The detailed analysis of the $1\,\mu\text{m/s}$ growth stage reveals several regions of various drift directions and speeds mapped in Figs. 18(a) and 18(b). The primary spacing is quite homogenous [Fig. 18(c)], except along some of the lines that border the different drifting regions where a lower primary spacing is observed. Along these specific lines, that correspond to converging boundaries, we also observe numerous cell eliminations. We attribute the origin of these different drifting regions to the $8\,\mu\text{m/s}$ growth stage during which the high pulling rate leads to more dendritic patterns combined to a highly concave front. Those two elements lead to a tilting of the growth direction with respect to the pulling axis, possibly due to the combined effect of crystalline misorientations, as previously discussed [46,47], and thermal gradient misorientation at concave growth front [38,48]. A crystalline misorientation induces translational drift when the thermal gradient is aligned to the pulling axis but combined to the misorientation of the thermal gradient due to concavity, of axial symmetry, a complex variation of tilting of the growth direction throughout the pattern is observed. After the pulling rate jump, even if the front has returned to a macroscopically flat shape, the multiple drifting areas indicate that the growth directions remain the ones selected before the jump. Consequently, in the $1\,\mu\text{m/s}$ growth stage, oscillations are inhibited by the high drift velocities.

IV. SUMMARY AND CONCLUSIONS

Experiments under low gravity conditions were carried out in the directional solidification insert of the DECLIC facility installed on board the International Space Station as part of a joint research program between CNES and NASA. The use of an organic transparent alloy (analog to metallic systems in terms of solidification behavior) in a large cylindrical crucible enabled the real-time and *in situ* observation of spatially extended patterns and microgravity enabled growth in a diffusive transport mode. These exceptional conditions allowed us to observe the dynamics of extended oscillating cellular patterns. The oscillations, observed in a narrow range of growth parameters, are manifested as a periodic variation of the apparent area of cells under top-view interface observation. We offer here a comprehensive analysis of the experimental characteristics of oscillating cell arrays, an experimental counterpart to the phase-field numerical study reported in [36].

In both experiments and simulations, spatially extended patterns are essentially hexagonal, with six-neighbor cells, but the density of defects, mainly five- and seven-neighbor cells, is high. This leads to a highly disordered pattern that keeps evolving during the whole experiment. This array disorder and its permanent dynamics, maintained by numerous tip-splitting events, are of major importance regarding the spatiotemporal characteristics of oscillation. Numerical simulations have shown that the lack of long range coherence of oscillation, which is expressed by the large dispersion of oscillation phases, is directly related to this disorder [36]. Yet, in small areas that present a local order of hexagonal or square arrangement maintained for several oscillation periods, a synchronization of the oscillation of neighboring cells may occur. In case of hexagonal tiling, three subarrays appear oscillating with a phase shift of roughly $\pm 2\pi/3$. A similar situation is obtained in case of square checkerboardlike organization near subgrain boundaries, with the two subarrays of the checkerboard oscillating in phase opposition. These modes of synchronization are typical for perfectly ordered patterns, as was demonstrated by numerical simulations, with a $\pm 2\pi/3$ phase shift for hexagons [33,34,36] or phase opposition for squares [34]. In our experiments and in our spatially extended simulations, such synchronization is always limited to few cells.

This behavior contrasts with observations of oscillating patterns in thin samples previously reported in [28], characterized by long-range coherence, suggesting that the lateral confinement imposes a higher order level, resulting in a longer range of coherence of oscillation. Another interesting difference between our observations in extended 2D patterns and the ones reported in confined samples is the effect of tip splitting and elimination. In confined samples, such events lead to the decrease of the amplitude of the oscillation that eventually stops: oscillating cells have to be in phase opposition to oscillate. This is clearly different in our case for which highly variable phase relations have been observed between adjacent cells so that any event modifying the local order can be accommodated in terms of oscillation, with or without phase shifting.

Oscillation occurs for a narrow range of parameters bounded, in our case, to the velocity range $2 < V/V_c < 6$ (V_c being the critical velocity for planar interface destabilization). The oscillation period is remarkably uniform throughout the entire array and significantly longer than the solutal diffusion time. The experimental oscillation period as a function of the pulling rate can be fitted by a power law similar to that found for breathing modes in thin samples [28].

Close to the higher limit of this velocity range, oscillation may occur only during the transient growth stage. Phase-field simulations have shown that sustained oscillations occur for a narrow range of primary spacings, close to the limits of stable cell branches, and in the close vicinity of the opening of spacing stability gap at a given temperature gradient. The transition from possible oscillating conditions in terms of control parameters (G, V) to stable nonoscillatory conditions is thus marked by the closure of the gap. As this gap closes for lower G, the amplitude of oscillations along continuous branches decreases with G within a range of about 5 K/cm below the stability limit. Moreover, while sustained oscillations of perfect hexagonal patterns exhibit a strong dependence of the oscillation amplitude to the primary spacing [36], in spatially extended disordered systems both experiments and simulations show that a variation of up to 50% of primary spacing does not affect the oscillation amplitude and period.

We evidenced the critical influence of pattern drift on oscillation inhibition. Such a drift consists of a component of growth velocity in the plane normal to the pulling axis, which is due to a misalignment between the $\langle 100 \rangle$ preferred growth direction and the pulling (thermal) axis; the direction and rate of drift depend on the misorientation angle and the pulling velocity [47]. In experiments, even if the single crystal seed has never been remelted, different subgrains are identified, probably due to a polygonization induced by thermal cycles. We showed that beyond a threshold of drift velocity—a function of the pulling velocity—oscillation is inhibited. The existence of this threshold can be explained by the perturbation of the dynamics of oscillation. Each tip drives its surrounding concentration field, and cell oscillation originates from an oscillation of this concentration field close to the tip. The drift of the tip perturbs this concentration field, inhibiting oscillation when the drift becomes significant. We proposed two criteria to define the threshold in drift velocity that inhibits oscillation. More systematic experimental and numerical studies remain needed to clarify this point.

The analysis of experiments with a change of pulling rate highlights the history dependence of microstructure dynamics. In these experiments, oscillations are not present when, instead of starting from rest, we jump from a higher velocity to a pulling rate corresponding to oscillating conditions when starting from rest. Several differences in the pattern characteristics and dynamics are highlighted. The most prominent difference is the observation after the velocity jump of several regions displaying high drift velocities, and again the inhibition of oscillation is attributed to pattern drifts.

To conclude, these microgravity experiments provided a unique opportunity to observe the formation and evolution of directionally solidified 2D extended arrays in diffusive transport conditions. Beyond the oscillatory modes described here, those experiments provided a large variety of results, covering a large number of topics. Ongoing investigations include the formation of multiplets, another secondary instability of the cellular pattern, previously predicted by numerical simulation and described in thin samples [49–52], as well as the dynamical selection of the primary spacing. Furthermore, 3D experiments were found to introduce additional unavoidable deviations from ideal models of solidification, which are negligible or controllable in thin samples, and which affect the microstructure characteristics and dynamics. For example, thermal analyses revealed a strong shifting of the thermal field while pulling, in contrast with the classical hypothesis of a growth in a frozen thermal field, especially during the first stages of growth and microstructure formation [40]. Preliminary studies of mechanisms of spacing adjustment have already highlighted the critical influence of the pattern drift, resulting from both macroscopic interfacial curvature and crystalline misorientations [53]. Understanding the influence of each of these elements is a promising challenge, which will allow us to address unique phenomena that arise during large-scale bulk solidification, from both numerical and experimental points of view.

ACKNOWLEDGMENTS

This research was achieved thanks to the support of CNES through the MISOL3D project (MIcrostructures de SOLidification 3D), NASA through Grants No. NNX16AB54G and No. NNX12AK54G, and Région PACA through the ENEMS project (Etude Numérique et Expérimentale des Microstructures de Solidification).

---

[1] M. Cross and H. Greenside, *Pattern Formation and Dynamics in Nonequilibrium Systems* (Cambridge University Press, New York, 2009).
[2] W. Kurz and D. J. Fisher, *Fundamentals of Solidification* (Trans Tech Pub, Zurich, 1998).
[3] J. A. Dantzig and M. Rappaz, *Solidification* (EPFL Press, Lausanne, 2009).
[4] K. A. Jackson and J. D. Hunt, Acta Metall. **13**, 1212 (1965).
[5] H. Esaka and W. Kurz, J. Cryst. Growth **72**, 578 (1985).
[6] M. A. Eshelman, V. Seetharaman, and R. Trivedi, Acta Metall. **36**, 1165 (1988).
[7] V. Seetharaman, M. A. Eshelman, and R. Trivedi, Acta Metall. **36**, 1175 (1988).
[8] W. Losert, B. Q. Shi, and H. Z. Cummins, Proc. Natl. Acad. Sci. USA **95**, 431 (1998).
[9] W. Losert, B. Q. Shi, and H. Z. Cummins, Proc. Natl. Acad. Sci. USA **95**, 439 (1998).
[10] A. Pocheau and M. Georgelin, Phys. Rev. E **73**, 011604 (2006).
[11] S. Akamatsu, G. Faivre, and T. Ihle, Phys. Rev. E **51**, 4751 (1995).
[12] S. Gurevich, A. Karma, M. Plapp, and R. Trivedi, Phys. Rev. E **81**, 011603 (2010).
[13] H. Jamgotchian, N. Bergeon, D. Benielli, P. Voge, B. Billia, and R. Guerin, Phys. Rev. Lett. **87**, 166105 (2001).
[14] T. Schenk, H. Nguyen-Thi, J. Gastaldi, G. Reinhart, V. Cristiglio, N. Mangelinck-Noel, H. Klein, J. Hartwig, B. Grushko, B. Billia, and J. Baruchel, J. Cryst. Growth **275**, 201 (2005).
[15] R. Trivedi, H. Miyahara, P. Mazumder, E. Simsek, and S. N. Tewari, J. Cryst. Growth **222**, 365 (2001).
[16] S. R. Coriell, D. T. J. Hurle, and R. F. Sekerka, J. Cryst. Growth **32**, 1 (1976).
[17] J. J. Favier and A. Rouzaud, J. Cryst. Growth **64**, 367 (1983).
[18] B. Billia, H. Jamgotchian, and H. Nguyen-Thi, J. Cryst. Growth **167**, 265 (1996).
[19] B. Caroli, C. Caroli, and B. Roulet, J. Cryst. Growth **76**, 31 (1986).
[20] R. Marcout, G. Raymond, B. Martin, G. Cambon, B. Zappoli, F. Duclos, S. Barde, D. Beysens, Y. Garrabos, C. Lecoutre, B. Billia, N. Bergeon, and N. Mangelinck, *DECLIC: A Facility to Investigate Fluids and Transparent Materials in Microgravity Conditions in ISS*, in: 57th International Astronautical Congress, Valencia, Spain (2006).
[21] G. Pont, S. Barde, B. Zappoli, F. Duclos, Y. Garrabos, C. Lecoutre, D. Beysens, B. Billia, N. Bergeon, N. Mangelinck, R. Marcout, and D. Blonde, *DECLIC: A Facility to Study Crystallization and Critical Fluids*, in: 60th International Astronautical Congress, Daejeon, Republic of Korea (2009).
[22] N. Bergeon, R. Trivedi, B. Billia, B. Echebarria, A. Karma, S. Liu, C. Weiss, and N. Mangelinck, Adv. Space Res. **36**, 80 (2005).
[23] N. Bergeon, A. Ramirez, L. Chen, B. Billia, J. H. Gu, and R. Trivedi, J. Mater. Sci. **46**, 6191 (2011).
[24] C. Misbah, *Dynamiques Complexes et Morphogenèse* (Springer, Paris, 2011).
[25] C. Misbah and A. Valance, Phys. Rev. E **49**, 166 (1994).
[26] N. Bergeon, D. Tourret, L. Chen, J. M. Debierre, R. Guerin, A. Ramirez, B. Billia, A. Karma, and R. Trivedi, Phys. Rev. Lett. **110**, 226102 (2013).
[27] P. E. Cladis, J. T. Gleeson, P. L. Finn, and H. R. Brand, Phys. Rev. Lett. **67**, 3239 (1991).
[28] M. Georgelin and A. Pocheau, Phys. Rev. Lett. **79**, 2698 (1997).
[29] P. Kopczynski, W. J. Rappel, and A. Karma, Phys. Rev. Lett. **77**, 3387 (1996).
[30] M. Zimmermann, A. Karma, and M. Carrard, Phys. Rev. B **42**, 833 (1990).
[31] A. Karma and A. Sarkissian, Metall. Mater. Trans. A **27**, 635 (1996).
[32] M. Ginibre, S. Akamatsu, and G. Faivre, Phys. Rev. E **56**, 780 (1997).
[33] K. Kassner, J. M. Debierre, B. Billia, N. Noel, and H. Jamgotchian, Phys. Rev. E **57**, 2849 (1998).
[34] M. Plapp and M. Dejmek, Europhys. Lett. **65**, 276 (2004).
[35] M. Perrut, S. Bottin-Rousseau, G. Faivre, and S. Akamatsu, Acta Mater. **61**, 6802 (2013).
[36] D. Tourret, J.-M. Debierre, Y. Song, F. L. Mota, N. Bergeon, R. Guérin, R. Trivedi, B. Billia, and A. Karma, Phys. Rev. E **92**, 042401 (2015).
[37] N. Bergeon, C. Weiss, N. Mangelinck-Noel, and B. Billia, Trans. Ind. Inst. Met. **62**, 455 (2009).
[38] C. Weiss, N. Bergeon, N. Mangelinck-Noel, and B. Billia, Phys. Rev. E **79**, 011605 (2009).
[39] M. Kurz, A. Pusztai, and G. Muller, J. Cryst. Growth **198**, 101 (1999).
[40] F. L. Mota, N. Bergeon, D. Tourret, A. Karma, R. Trivedi, and B. Billia, Acta Mater. **85**, 362 (2015).
[41] See Supplemental Material at http://link.aps.org/supplemental/10.1103/PhysRevE.95.012803 for $V = 0.75$ and $1\,\mu\mathrm{m/s}$ ($G = 19\,\mathrm{K/cm}$).

[42] B. Billia, H. Jamgotchian, and H. Nguyen-Thi, Metall. Trans. A: Phys. Metall. Mater. Sci. **22**, 3041 (1991).

[43] P. Cerisier, S. Rahal, and B. Billia, Phys. Rev. E **54**, 3508 (1996).

[44] N. Noël, H. Jamgotchian, and B. Billia, J. Cryst. Growth **187**, 516 (1998).

[45] F. L. Mota, L. M. Fabietti, N. Bergeon, L. L. Strutzenberg, A. Karma, B. Billia, and R. Trivedi, J. Cryst. Growth **447**, 31 (2016).

[46] S. Akamatsu and T. Ihle, Phys. Rev. E **56**, 4479 (1997).

[47] J. Deschamps, M. Georgelin, and A. Pocheau, Phys. Rev. E **78**, 011605 (2008).

[48] C. Weiss, N. Bergeon, N. Mangelinck-Noel, and B. Billia, Mater. Sci. Eng. A: Struct. Mater. Prop. Microstruct. Process. **413**, 296 (2005).

[49] H. Jamgotchian, R. Trivedi, and B. Billia, Phys. Rev. E **47**, 4313 (1993).

[50] E. Brener, H. Müller-Krumbhaar, Y. Saito, and D. Temkin, Phys. Rev. E **47**, 1151 (1993).

[51] A. Ludwig, Phys. Rev. E **59**, 1893 (1999).

[52] W. Losert, D. A. Stillman, H. Z. Cummins, P. Kopczynski, W. J. Rappel, and A. Karma, Phys. Rev. E **58**, 7492 (1998).

[53] N. Bergeon, F. L. Mota, L. Chen, D. Tourret, J. M. Debierre, R. Guerin, A. Karma, B. Billia, and R. Trivedi, IOP Conf. Ser.: Mater. Sci. Eng. **84**, 012077 (2015).